Effect of inlet leakage flow on the instability in a radial vaneless diffuser

M. Fan, Antoine Dazin, G. Bois, Francesco Romano

Effect of inlet leakage flow on the instability in a radial vaneless diffuser

M. Fan,[1] A. Dazin,[1] G. Bois,[1] and F. Romanò[1]
Univ. Lille, CNRS, ONERA, Arts et Métiers Institute of Technology, Centrale Lille, UMR 9014-LMFL-Laboratoire de Mécanique des Fluides de Lille - Kampé de Fériet, F-59000, Lille, France

(*Electronic mail: meng.fan@ensam.eu)

(Dated: 30 October 2023)

The internal flow structures in a vaneless diffuser of a radial pump are experimentally and numerically investigated. Numerical simulations are used for investigating the prominent features of the fluid flow in the vaneless diffuser upon a change of the flow rate and of the impeller-to-diffuser radial gap. Comparisons between experimental and numerical results on the overall pump and diffuser performances are presented and discussed. The influence of inlet diffuser leakages on the development of flow instabilities is specifically addressed, owing to the remarkable impact that a small impeller-to-diffuser radial gap can have on the diffuser flow. Highlights on the rotating instabilities in terms of stall cell number and propagation velocity at design and off-design conditions are the main focus of this study and will be investigated using the numerical and experimental results post-processed by fast Fourier transform (FFT) and wavelet analysis.

I. INTRODUCTION

The pressure recovery in radial compressors or pump vaneless diffusers is often subject to performance limitations. This is typical of compressors or pumps operating at partial flow rates, i.e., at flow rates lower than the design flow rate. Such limitations are induced by flow separation phenomena usually classified in singular and ordinary flow separations as reported by Japikse [1]. The former, on the one hand, occurs because a too-large mean deceleration is produced by the vaneless diffuser. The latter, on the other hand, is more common due to the local overturning of the streamlines close to the wall.

The local decrease of kinetic energy is the main cause of separation as explained by several authors (see e.g. Jansen [2]). Both types of performance limitations refer to static stall configurations that occur in a specific fixed location in the machine. However, they may initiate peculiar rotating instabilities that in vaneless diffusers are commonly termed rotating stall in order to point out the dynamic character of the stall.

Dynamic stall is an important subject, far more difficult to report on than static stall. Dynamic stall patterns are, in fact, not fixed in a given reference frame as it happens for the static stall. Indeed, they rotate in the machine system at some fraction of the machine's rotational speed. Such dynamic conditions can exist in different components in all kinds of turbomachines, depending on the specific speed and design. However, in radial flow machines (pumps, fans, and compressors) they are mostly observed in configurations for which the machine is equipped with a vaneless diffuser, which turns out to be the most sensitive component with respect to such instabilities. They are crucial to control or avoid as they can induce vibrations and initiate or amplify surge conditions for the whole machine system.

Based on Jansen's work, two papers from Senoo and Kinoshita [3] and Senoo, Kinoshita, and Ishida [4] critically evaluated the conditions for the onset of reverse flow in a vaneless diffuser. In their first reference, Abdelhamid, Colwill, and Barrows [5] have reported dynamic measurements in a vaneless diffuser that helped unravel the underlying physics of dynamic stall phenomena. They observed that the dynamic stall condition develops in a gradual manner in the diffuser space as the machine flow rate is decreased. Their work was extended, considering the diffuser geometry variations[6]. These unforced rotating instabilities have been theoretically investigated using two different approaches: a 3D wall boundary layer stability analysis[7] and a two-dimensional inviscid approach only assuming a core flow region in the vaneless diffuser hub-to-shroud sections[8,9] in case of wide diffuser ratios, i.e. for diffusers whose ratio between the height (b_2) and the outlet-to-inlet diffuser radius difference ($R_4 - R_3$) is $\Gamma = (R_4 - R_3)/b_2 \lesssim \mathcal{O}(1)$.

The results show that the stability limit for wide vaneless diffusers can be expressed in terms of the critical flow angle at the diffuser inlet. The critical flow angle is also found to depend on the diffuser radius ratio, as well as on the number of stall cells. In accordance with the core flow assumption, the effect of the wall boundary layers is found to be negligible. However, it is expected that by including the wall boundary layer effects into the 2D inviscid model developed by Tsujimoto, Yoshida, and Mori [8], the characteristics of the most dangerous mode predicted by their two-dimensional model may change, certainly in terms of the detailed unstable pattern, and potentially either in terms of the number of stall cells or of their propagation speed, if not of the onset of instability only expressed by the critical flow angle. Within similar two-dimensional working hypotheses, an additional study presented by Ljevar, de Lange, and van Steenhoven [10] also suggests that the usual "jet and wake" pattern delivered by impellers has no influence on the development of these rotating instabilities at low flow rates.

In a previous study, an identification of the instabilities developing in the radial vaneless diffuser of interest for our study has been performed numerically and experimentally by Pavesi *et al.* [11] for two partial flow rates. Depending on the operating conditions, Pavesi *et al.* [11] identified either a rotating stall in form of a single mode or two competing modes leading to an intermittency phenomenon (see also Dazin [12]). It is however still unclear if a specific mechanism is responsible for driving

the switch from one mode to the other one, or if the phase space of the unstable flows at low flow rates is chaotically arranged around two connected attractors (the two modes). In the latter case, no specific mechanism would be required to switch from one mode to another and the intermittency would be the result of an enhanced sensitivity of the system to small perturbations near saddle or hyperbolic points in phase space. Additionally, Pavesi *et al.* [11] reported that to capture correctly the instability, it was necessary to include in the simulations the effect of the leakage flow occurring between the diffuser and the runner, even for small impeller-to-diffuser radial gaps. The instability thus seems to be very sensitive to the diffuser inlet flow conditions.

For the present paper, the same pump model of Pavesi *et al.* [11] is investigated experimentally, and three conceptually complementary leakage flow configurations are considered numerically, either (i) sealing the impeller-to-diffuser gap (zero-leakage case), (ii) leaving a radial gap open to the surroundings from which air can flow inside the diffuser (positive-leakage case), or (iii) including a fixed carter that connects the diffuser inlet to the section just before the impeller inlet leaking air from the diffuser to the impeller inlet (negative-leakage case) through a small radial gap. The key point of this work is to study the rotating instability inside the vaneless diffuser, as even small radial gaps between the impeller and the diffuser can significantly affect the flow. Besides, we will consider the hypothesis of a centrifugal-type mechanism as an origin for the rotating stall, and discuss the low-flow-rate instability in terms of the lift-up and flow deceleration mechanisms.

The paper is therefore structured as follows: Section II introduces the experimental apparatus and measuring techniques, Sec. III defines the mathematical model of the incompressible flow and presents the discretization employed to numerically solve the Navier–Stokes system. The results of the URANS simulations are presented in Sec. IV and, finally, in Sec. V the results are summarized and conclusions are drawn.

II. EXPERIMENTAL APPARATUS AND PROCEDURE

A. Experimental Apparatus

The experimental vaneless diffuser test case corresponds to the so-called Société Hydrotechnique de France (SHF) pump which is an enlarged air model (impeller with diffuser and no volute) specifically built to allow experimental optical access for unsteady flow analysis with well-defined constant outlet pressure boundary conditions as already presented by Dazin [12], Wuibaut *et al.* [13]. Such an experimental test rig includes a radial impeller coupled with a vaneless diffuser as shown in fig. 1 (a). The main parameters of the radial impeller and vaneless diffuser are given in tab. I.

This arrangement allows for positive-leakage flow entering the vaneless diffuser inlet because of the radial gap between the outlet rotating impeller section and the fixed inlet diffuser one. This leakage flow configuration is representative of radial ventilation and extraction devices whose outlet static pressure

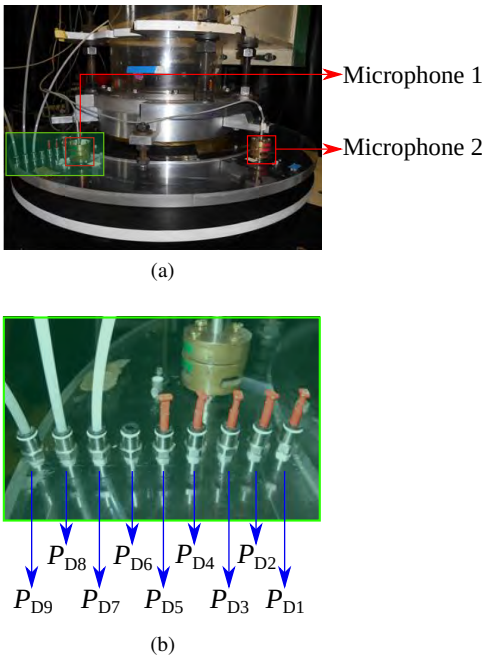

FIG. 1. Experimental set-ups of the centrifugal pump with (a) two microphones mounted on it, and (b) zoom-in view of nine static pressure taps installed on the vaneless diffuser (green rectangle in (a)).

TABLE I. Main geometrical characteristics of the impeller and diffuser model.

SHF impeller characteristics		
R_1	Tip inlet radius	141.1 mm
R_2	Outlet radius	257.5 mm
b_2	Outlet width	38.5 mm
Z	Number of blades	7
β_{2c}	Outlet blade angle	22.5 °
K	Mean blade thickness	9 mm
Q_d	Design flowrate (1200 rpm)	0.236 m^3/s
$Re = {R_2}^2 \omega_{imp}/\nu$	Reynolds number (Q/Q_d = 1.0, N = 1200 rpm)	5.52×10^5

Vaneless diffuser characteristics		
	Inlet radius (zero-leakage)	257.5 mm
R_3	Inlet radius (negative-leakage)	260.075 mm
	Inlet radius (positive-leakage)	260.075 mm
R_4	Outlet radius	385.5 mm
b_3	Constant width	38.5 mm

is at atmospheric conditions. Thus, all local static pressures inside the whole pump are always below the atmospheric pressure. The main difference with conventional radial pump designs is that they usually make use of a carter connecting the diffuser inlet and the inlet-pipe outlet, therefore providing a casing to the impeller. Hence, differently from our experimental setup, for conventional radial pumps, part of the outflow rate at the impeller outlet returns to the impeller inlet driven by the pressure gradient. This corresponds to a negative-leakage flow for the diffuser and is generally represented by the so-

called pump volumetric efficiency, expressing that the outlet pump flow rate is lower than the impeller flow rate.

B. Measuring techniques

Our experimental setup is equipped with nine steady pressure taps which are flush-mounted on the diffuser wall along a radial line. The probes are equally spaced from $r = 264\,\text{mm}$ to $r = 384\,\text{mm}$ (see fig. 1(b)). Therefore, the diffuser performance is characterized based on the pressure recovery from the inlet to the outlet of the diffuser. The uncertainty of these measurements is estimated to be $\pm 2\,\text{Pa}$. To ensure stable pump inlet flow condition, a tank, equipped with a honeycomb flow straightener, was placed in front of the suction pipe. A set of changeable diaphragms (with different inlet diameters) is available to be installed at the tank inlet in order to adjust the flow rate Q.

Two Brüel & Kjaer (Nærum, Denmark) condenser microphones (Type 4135) were used to measure the unsteady pressure fluctuation. They are flush-mounted at the same radial location, i.e. at $r = 320\,\text{mm}$, on the diffuser wall but with an angular shift of $\Delta\theta = 60^\circ$. This allows us to detect the instabilities occurring in the vaneless diffuser and characterize their propagation velocity. The measurement uncertainty for these probes is less than 1%. The data were acquired by LMS Test Xpress (SIEMENS, Munich, Germany) for the total time of 600 s sampled with the frequency of 4096 Hz.

The experiments were performed in the air for a wide range of flow rate ratios relative to design condition $Q/Q_\text{d} \in [0.26,\ 1.53]$, where Q and Q_d denote the actual and the design flow rates measured at the inlet pipe at constant rotating speed $N = 1200\,\text{rpm}$ (i.e. $\omega_\text{imp} = 125\,\text{rad/s}$). More details of this experimental test rig can be found in previous studies presented by Dazin [12], Dazin *et al.* [14] that operate the same apparatus. We further stress that, due to the leakage effects, the flow rate of the diffuser and of the impeller may differ from Q as they require the evaluation of the leakage flow at the impeller and diffuser inlet. More details about such corrections are discussed in Sec. IV.

III. COMPUTATIONAL PROCEDURE

A. Computational domain

Figure. 2(a) depicts the computational domain consisting of an inlet pipe (blue), the pump impeller (gray), the diffuser (violet) and a radial outflow box (dark pink) introduced at the outlet of the diffuser in order to avoid enforcing the outflow boundary conditions too close to the pump. The geometry of the numerical model matches the experimental set-up (fig. 1) characterized in tab. I. The inlet boundary conditions are set at the top of the circular straight pipe (inlet pipe) whose length H_c is equal to ten times of the impeller tip inlet radius R_1. The outlet conditions are given at the boundaries of the outflow box (dark pink) of height H_b and radius R_4, where $H_b/b_3 = 15$ and $R_4/R_3 = 3$. In order to investigate the effect of the leakage flow on the radial diffuser flow, three conceptually different leakage configurations are numerically simulated. They are termed zero-, negative- and positive-leakage case as they refer to the leakage flow entering the diffuser:

Zero-leakage: corresponds to a simplified configuration for which there is no leak between the impeller and the vaneless diffuser as the radial gap between impeller and diffuser is set to zero (see fig. 2(b)). Also, between inlet-pipe outlet and impeller inlet we consider no axial gaps;

Negative-leakage: corresponds to a usual pump configuration that allows leakage flow from outlet to inlet sections of the impeller thanks to the casing around the impeller. Consequently, a radial gap $L = R_3 - R_2$ is introduced as shown in fig. 2(c). The distance from the casing wall to the impeller is constantly equal to the gap width L;

Positive-leakage: shown in fig. 2(d), qualitatively reproduces the experimental geometry in the corresponding numerical simulations. Note that the experimental radial gap (1 mm) and the numerical one (3 mm) are different. In our numerical simulations, the radial gap between the impeller and the diffuser is enlarged on purpose to clearly highlight the influence of the positive-leakage flow. The axial gap between the inlet-pipe outlet and the impeller inlet is neglected. All the comparisons between experiments and numerical performance are considered for the positive-leakage case, employed for discussion and validation of our numerics.

B. Governing Equations

The incompressible viscous fluid flow in a radial pump is formulated by employing the Unsteady Reynolds-Averaged Navier–Stokes (URANS) equations:

$$\frac{\partial \vec{U}}{\partial t} + (\vec{U}\cdot\nabla)\vec{U} + \nabla P = \nabla\cdot(2\nu\vec{\vec{S}} - \vec{\vec{\tau}}), \quad \nabla\cdot\vec{U} = 0, \qquad (1)$$

where $\vec{U} = \vec{U}(\vec{x};\ t) = (U_1, U_2, U_3)$ denotes the mean part of the velocity vector, $(\vec{x};\ t) = (x_1, x_2, x_3;\ t)$ are the spatial and temporal coordinates, $P = P(\vec{x}, t)$ is the mean pressure field, ν the kinematic viscosity, $\vec{\vec{S}} = \frac{1}{2}(\nabla\vec{U} + \nabla^T\vec{U})$ is the mean rate of the strain tensor, $\vec{\vec{\tau}}$ is the Reynolds stress tensor, and ν_T is the turbulent viscosity (see Wilcox [15], Sváček, Louda, and Kozel [16] for details).

As the main focus of this study is on the fully-developed instabilities, the initial startup of the pump is skipped by initializing all the URANS simulations out of a corresponding

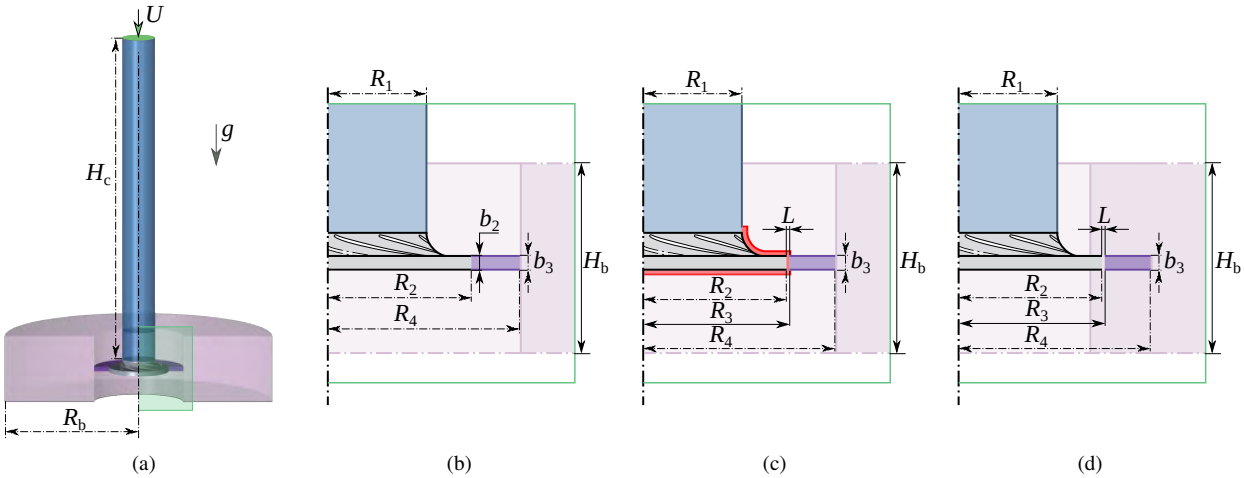

FIG. 2. Schematic of (a) the entire computational domain for the radial flow pump and zoom-in view for the three configurations: (b) zero-, (c) negative-, and (d) positive-leakage case.

steady simulation (RANS). Since the frequencies of the stall phenomena of interest in this study are lower than the rotational speed of the impeller, a long physical simulation time t_{fin} is required to resolve the low-frequency range. Therefore, $t_{\text{fin}} = 70T$, where T is one impeller revolution period, was set for all URANS simulations to make sure that all the results presented hereinafter are at fully-developed conditions. All the following results are therefore presented at $t = t_{\text{fin}}$ and all the phase-averaged results employed to characterize rotating patterns are produced advancing the simulation starting from $t = t_{\text{fin}}$.

C. Turbulence modeling

The shear-stress transport (SST) $k-\omega$ turbulence model is used to model the Reynolds stress tensor because it accounts for the transport of the principal turbulent shear stress. Such a feature makes the $k-\omega$ SST model a suitable choice for the centrifugal pump over both, the standard $k-\varepsilon$ and the realizable $k-\varepsilon$ models. Other modifications to the standard $k-\omega$ SST model have been proposed in literature[17] to include a cross-diffusion term in the $\omega-$equation and a blending function to ensure that the model equations behave appropriately in the near-wall and far-field zones[18]. In this study, we employ one of such modified $k-\omega$ SST models, following the formulation of Menter[19]. It is known that turbulence models based on the Boussinesq hypothesis can face modeling issues when attempting to solve for rapidly rotating flows with strongly curved streamlines. The model we selected has been proven to have a reasonably stable, robust, and time-efficient capability to predict global performance and capture the key flow features in centrifugal pump simulations[20]. This is also confirmed by several examples[21–24] in the literature and validated by experiments.

The corresponding turbulent kinetic energy k equation is given by

$$\frac{\partial k}{\partial t} + (\vec{u}\cdot\nabla)k = P_k - \beta^*\omega k + \nabla\cdot[(\nu+\sigma_k\nu_T)\nabla k], \quad (2)$$

and for turbulence-specific dissipation rate ω, it yields

$$\begin{aligned}\frac{\partial \omega}{\partial t} + (\vec{u}\cdot\nabla)\omega =& \alpha S^2 - \beta\omega^2 + \nabla\cdot[(\nu+\sigma_\omega\nu_T)\nabla\omega] \\ &+ 2(1-F_1)\frac{\sigma_{\omega 2}}{\omega}\nabla k\cdot\nabla\omega,\end{aligned} \quad (3)$$

where the production term P_k is given by

$$P_k = \nu_T\vec{\vec{S}}(u):\vec{\vec{S}}(u), \quad (4)$$

and the blending function F_1 is defined by

$$F_1 = \tanh\left\{\left\{\min\left[\max\left(\frac{2\sqrt{k}}{\beta^*\omega y}, \frac{500\nu}{y^2\omega}\right), \frac{4\rho\sigma_{\omega 2}k}{CD_{k\omega}y^2}\right]\right\}^4\right\}, \quad (5)$$

with $CD_{k\omega} = \max\left(2\rho\sigma_{\omega 2}\frac{1}{\omega}\nabla k\cdot\nabla\omega, 10^{-10}\right)$, y being the normal distance to the nearest wall. Finally, the turbulent eddy viscosity is defined as

$$\nu_T = \frac{\alpha_1 k}{max(\alpha_1\omega, SF_2)}, \quad (6)$$

where F_2 is a second blending function:

$$F_2 = \tan\left[\left[\max\left(\frac{2\sqrt{k}}{\beta^*\omega y}, \frac{500\nu}{y^2\omega}\right)\right]^2\right]. \quad (7)$$

Further details of the modeling techniques and the constants $(\beta, \beta^*, \sigma_k, \sigma_{\omega 2}, \alpha_\omega)$ of this model can be found in Menter[19].

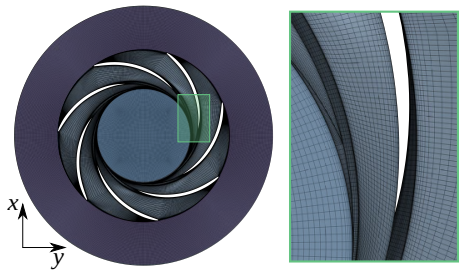

(a) Top view

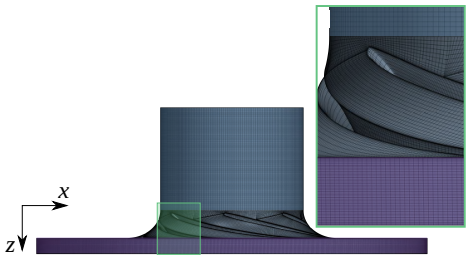

(b) Side view

FIG. 3. Top (a) and side (b) view of a typical mesh of the zero-leakage case used in URANS simulations (The right part of each figure is a zoom-in view of the green rectangle region marked in the left part).

D. Mesh and time step

Hexahedral cells are chosen for meshing, which is proven to be less costly and less diffusive than tetrahedral cells, especially at the boundary layer. The commercial software ANSYS ICEM CFD is used for generating the mesh. The multi-block structure used in ICEM-CFD makes the mesh generation flexible and accurate. The inlet pipe (of height $H_c = 20R_1$) is split into two parts, one of which is long enough before the impeller to stabilize the inlet flow, while the second short part of the inlet pipe (of height $\frac{1}{10}H_c$) shares an interface with the impeller. The grid in the short part of the inlet pipe, impeller, and vaneless diffuser regions is finer as shown in fig. 3. The grid used in the long part of the inlet pipe and the outflow radial box regions is coarser as these parts of the computational domain are included solely to avoid enforcing inlet and outlet boundary conditions too close to the impeller and the diffuser, respectively. Once the mesh is generated, the mesh converter `fluent3DmeshToFoam` is used to convert the mesh into the format in use by OpenFOAM. The postulated mathematical problem is solved by the open-source software OpenFOAM, and details of the OpenFOAM solvers we used can be found in Appendix A.

In the near-wall regions, the mesh is refined using an expansion ratio of 1.5. Thus, the values y^+ are kept at approximately $y^+ \approx 1$ near the walls in the short inlet pipe, impeller, and diffuser regions. The corresponding y^+ value is less than $y^+ < 10$ near the long pipe wall as a coarser mesh is used for this region. The Menter $k-\omega$ SST model used in the current study has an accurate and robust near-wall treatment. Referring to the near-wall grid density, this model can automatically shift from a low-Re formulation to wall functions (Menter *et al.*[17], Invigorito, Cardillo, and Ranuzzi[25]). This allows us to use the correct range of y^+. Based on a grid number independence verification, a total mesh number of 2.3M finite volumes was selected for the following numerical simulations, more details are given in Appendix B.

In order to assure the required numerical accuracy and to limit the total computational cost, a time step Δt, corresponding to $\Delta\theta = 0.5^\circ$ of the runner revolution, i.e. $\Delta t = \Delta\theta/(2\pi\omega_{\text{imp}}) \times 2\pi/180^\circ$, was selected. This is in agreement with several literature studies[26] that suggest $\Delta\theta \leq 1^\circ$. Our choice for the Δt leads to a characteristic Courant number of $C = |U|\frac{\Delta t}{\Delta x} \approx 0.05$, where Δx is the local mesh size. This value is estimated for the cells in the bulk region of the diffuser, which is the major focus of this study. Its estimate is based on the theoretical value of the diffuser inlet velocity and the length scale resulting from the volume of the mesh elements. By a-posteriori computation of the Courant number, all our simulations at nominal flow rate are carried out with an averaged Courant number for the whole domain of $\overline{C} = 0.0075$.

E. Boundary conditions

Dirichlet, Neumann, or mixed conditions are set at the boundaries of the computational domain. The inlet velocity is specified by a Dirichlet boundary condition termed `flowRateInletVelocity` in OpenFOAM, which prescribes an inlet velocity corresponding to a pre-set value of inlet flow rate Q. For fixed walls, the no-slip boundary condition is employed (`noSplip` in OpenFOAM), whereas the option `rotatingWallVelocity` is used for the rotating walls in order to specify the constant rotation rate of the impeller. The `inletOutlet` routine of OpenFOAM is employed with the static pressure P = 0 Pa at the outflow box set a boundary condition that enforces: (i) a Neumann-type zero-gradient boundary condition for the velocity field if the fluid flows out of the computational domain and (ii) a Dirichlet-type boundary condition if the velocity field in the domain would require a fluid inflow, which is obtained by extrapolation from the bulk[27]. Distinct mesh zones are coupled at their interfaces using the coupling condition `cyclicAMI`, which applies to the interfaces between: (i) inlet pipe and impeller, (ii) impeller and diffuser, and (iii) diffuser and outflow box. All the OpenFOAM routines used to model the boundary conditions are summarized in tab. II.

The inlet value for the turbulent kinetic energy k_{in} is estimated by

$$k_{\text{in}} = \frac{3}{2}(I|u_{\text{ref}}|)^2, \tag{8}$$

where u_{ref} is a reference velocity given by the radial velocity at the suction pipe inlet and I is the turbulence intensity defined by

$$I = 0.16(Re)^{-\frac{1}{8}}. \tag{9}$$

TABLE II. Boundary condition types used in OpenFOAM v1912.

Boundary surface	p	U	k	ω
Inlet	`zeroGradient`	`flowRateInletVelocity`	`fixedValue`	`fixedValue`
Outlet	`fixedValue`	`inletOutlet`	`inletOutlet`	`inletOutlet`
Interfaces	`cyclicAMI`	`cyclicAMI`	`cyclicAMI`	`cyclicAMI`
Fixed walls	`zeroGradient`	`noSlip`	`fixedValue`	`omegaWallFunction`
Rotating walls	`zeroGradient`	`rotatingWallVelocity`	`fixedValue`	`omegaWallFunction`

The turbulent specific dissipation rate ω_{in} is calculated as

$$\omega_{\text{in}} = \frac{k_{\text{in}}^{0.5}}{C_{\mu}^{0.25} l}, \tag{10}$$

where C_{μ} is a constant equal to 0.09, and l is a reference length scale, i.e. the inlet pipe diameter in our simulations. Along the walls, we set

$$k_{\text{wall}} = 0, \qquad \omega_{\text{wall}} = \frac{60\nu}{0.075 y_1^2}, \tag{11}$$

where the subscript 'wall' denotes the boundary condition for the turbulence model at the pump walls, and y_1 is the distance from the first cell center to the closest wall[28].

IV. RESULTS

A. Comparison of the overall performance

The performance of the pump, encompassing the impeller and the diffuser, as well as the diffuser performance evaluated in terms of static pressure rise are obtained from the URANS simulations and compared with the experimental results respectively in figs. 4(a,b). Note that the volumetric flow rate Q is measured far upstream of the pump inlet, i.e. at the upstream section of the inlet pipe. The performance curve of the positive-leakage case, which is the closest configuration to the experimental setup, approaches the experimental ones the most over the whole operating range. The performance curve of the zero-leakage case is slightly above the experimental results, while the performance for the negative-leakage case lies below. Most of the experimental results are between the numerical results of the zero- and positive-leakage case, with a maximum deviation of about 5% for both cases. This is expected as the effective leakage flow of the experiments is within the positive- and the zero-leakage cases simulated by URANS. Concerning the negative-leakage case, the pressure difference between the impeller outlet and the impeller inlet section leads to a leakage flow going out at the impeller-diffuser radial gap, feeding back to the impeller inlet plane. This results in an increment of the flow rate in the impeller, leading to a larger deviation in the pump performance curve when comparing the negative-leakage case and the experimental results. Due to the presence of experimental positive inlet leakage, the flow rate inside the vaneless diffuser Q_{D} is bigger than the actual Q value which is close to the impeller flow rate Q_{I}. Figure 5 depicts the estimated leakage flow rate ratio proposed by Heng, Dazin, and Ouarzazi[9], Heng *et al.*[29,30] and the one obtained from our URANS simulations. The numerical positive-leakage value is about three times bigger than the experimental one, which is in accordance with the gap ratio that has been chosen to be three times bigger than in the experiments for our URANS simulations. This effect is taken into account and the corrected performance curves based on the flow rate increment in the impeller are plotted in fig. 6(a). The corresponding simulation results of negative-leakage get closer to the experimental ones taking into account such a correction.

The diffuser performance is shown in fig. 4(b). With the same consideration on the leakage effect proposed above, the results of the positive-leakage case are in better agreement with the experimental data as shown in fig. 6(b). To investigate more in-depth the diffuser behavior with three different geometries and to better compare the experiment and numerical simulation results, the diffuser pressure recovery curves at the design flow rate $Q/Q_{\text{d}} = 1.00$ and under fully-developed low-flow-rate rotating stall conditions at $Q/Q_{\text{d}} = 0.25$ are plotted in fig. 7. The URANS simulations well predict the experimental diffuser performance.

B. Flow configuration of the zero-leakage case

The flow field obtained from URANS simulations of the zero-leakage case at the design flow rate is firstly presented in this section since it corresponds to the simplest case without the influence of the leakage flow. Note that in all the following color maps, the velocities and static pressures are nondimensionalized by

$$\hat{U}_* = \frac{U_*}{U_2}, \qquad \hat{P} = \frac{P}{\frac{1}{2}\rho {U_2}^2}, \tag{12}$$

where $* \in \{r, \theta, z\}$, and $U_2 = \omega_{\text{imp}} R_2$ is a characteristic velocity in this problem.

Figures 8 depict the instantaneous static pressure and velocity magnitude over the meridian plane ($x = 0$). The static pressure distribution shown in fig. 9(a) depicts the 7-periodic pattern in accordance with the impeller blade number. Hub to shroud pressure remains almost constant for a given radial and tangential location. Owing to the presence of the

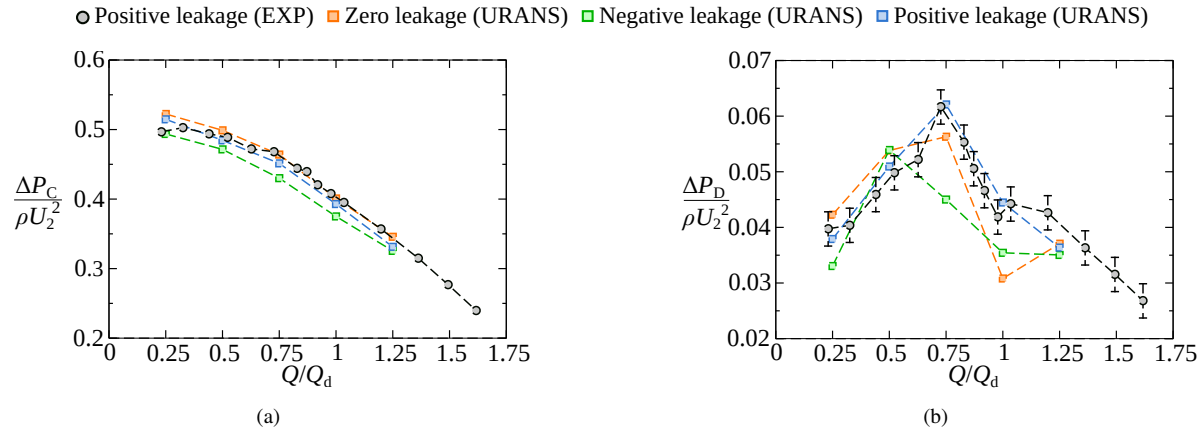

FIG. 4. Performance curves of (a) pump and (b) diffuser for three different geometries obtained from experimental and URANS numerical simulation results.

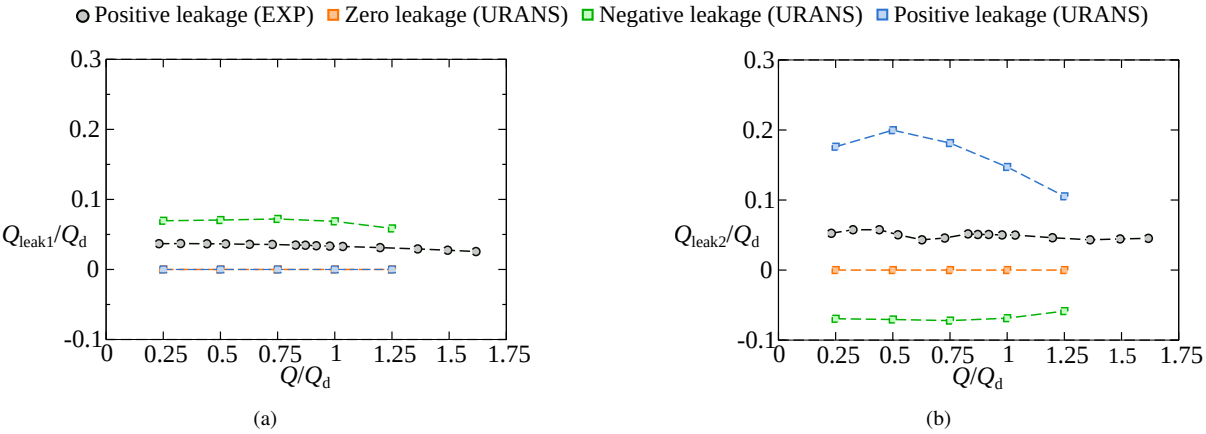

FIG. 5. (a) Inlet-impeller leakage flow rate Q_{leak1} and (b) impeller-diffuser leakage flow rate Q_{leak2} versus the flow rate of the pump Q.

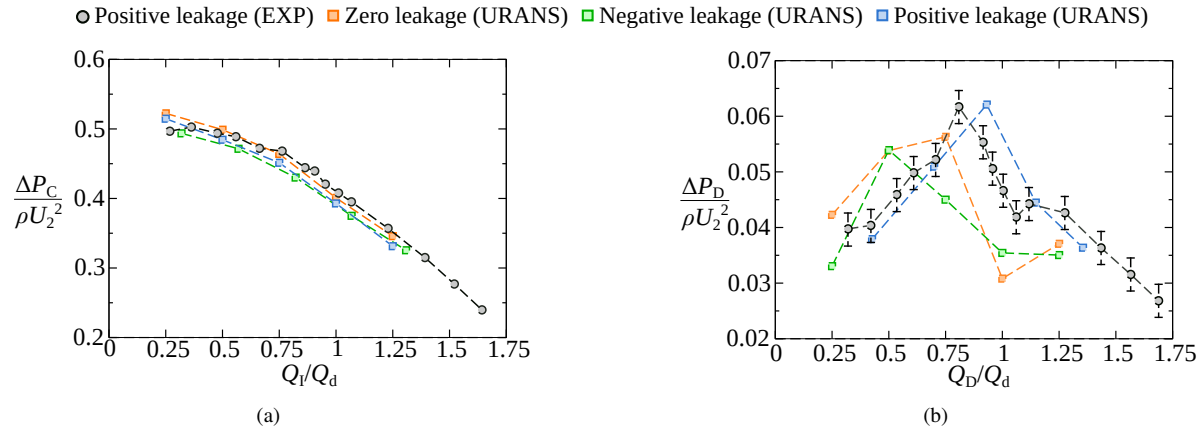

FIG. 6. Corrected performance curves of (a) pump and (b) diffuser for three different geometries obtained from experimental and URANS numerical simulation results.

no-slip boundary condition over the rotating walls, the instantaneous velocity field differs from hub to shroud, as shown in fig. 9(b). A bigger velocity magnitude is observed close to the shroud section which corresponds to the combined effects of the meridian impeller shape and the hub diffuser limiting the deceleration as already observed in previous research papers[11].

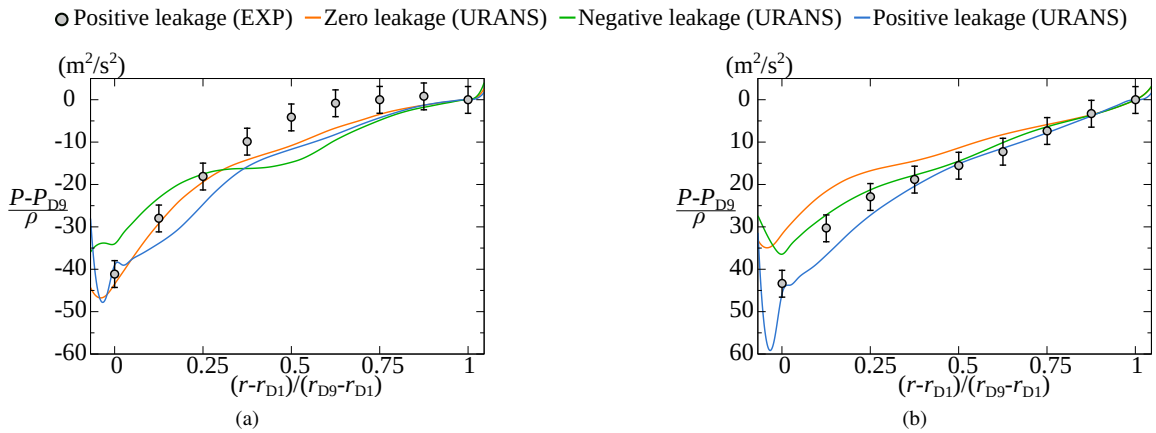

FIG. 7. Diffuser pressure recovery curves of three different geometries at the (a) design condition $Q/Q_{\mathrm{d}} = 1.00$, and (b) stall condition $Q/Q_{\mathrm{d}} = 0.25$.

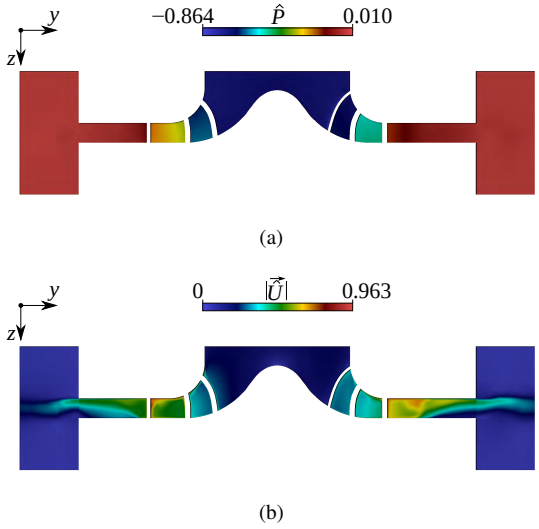

FIG. 8. Colour Maps of instantaneous (a) static pressure and (b) velocity magnitude distribution over the meridian section (x = 0) of the pump at the design flow rate $Q/Q_{\mathrm{d}} = 1.00$ obtained by the URANS simulation.

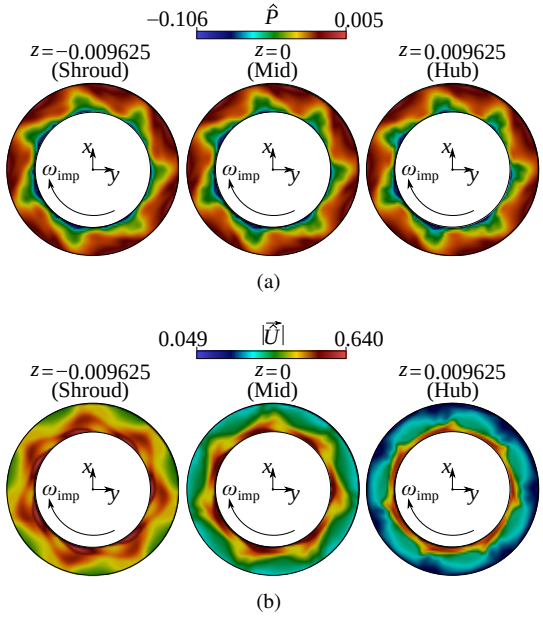

FIG. 9. Colour Maps of instantaneous (a) static pressure and (b) velocity magnitude distribution over 3 different heights of the diffuser at the design flow rate $Q/Q_{\mathrm{d}} = 1.00$ obtained by the URANS simulation.

C. Instability at the design flow rate

1. *Instability characteristics of the zero-leakage case*

To investigate more in-depth the flow field at the design flow rate $Q/Q_{\mathrm{d}} = 1.00$, the azimuthal arithmetic-averaged color maps at the meridian section of the diffuser and the instantaneous color maps at three different heights of the diffuser are plotted in fig. 10 for the static pressure and the three different velocity components of the zero-leakage case. Under the influence of the non-uniform swirling inflow coming from the rotating impeller, a pronounced flow separation, and a significant reverse flow can be detected close to the hub side starting from the diffuser inlet and growing further in the entire diffuser hub area (fig. 10(a)). The 7-periodic flow pattern is observed very clearly in all color maps, especially in the static pressure and the radial velocity field at different heights of the diffuser (fig. 10(b–d)). The reverse flow area observed in fig. 10(a) further reinforces the radial velocity component due to blockage effects.

A complementary analysis is carried out using a Fourier decomposition of the cross-power spectrum using the URANS simulation results from two numerical probes located at the mid-radial distance of the diffuser shroud wall. These two numerical probes have an angular phase shift of 60°. In fact, the analysis of the cross-power spectra of two pressure probes located at the same radius but at two different angular positions

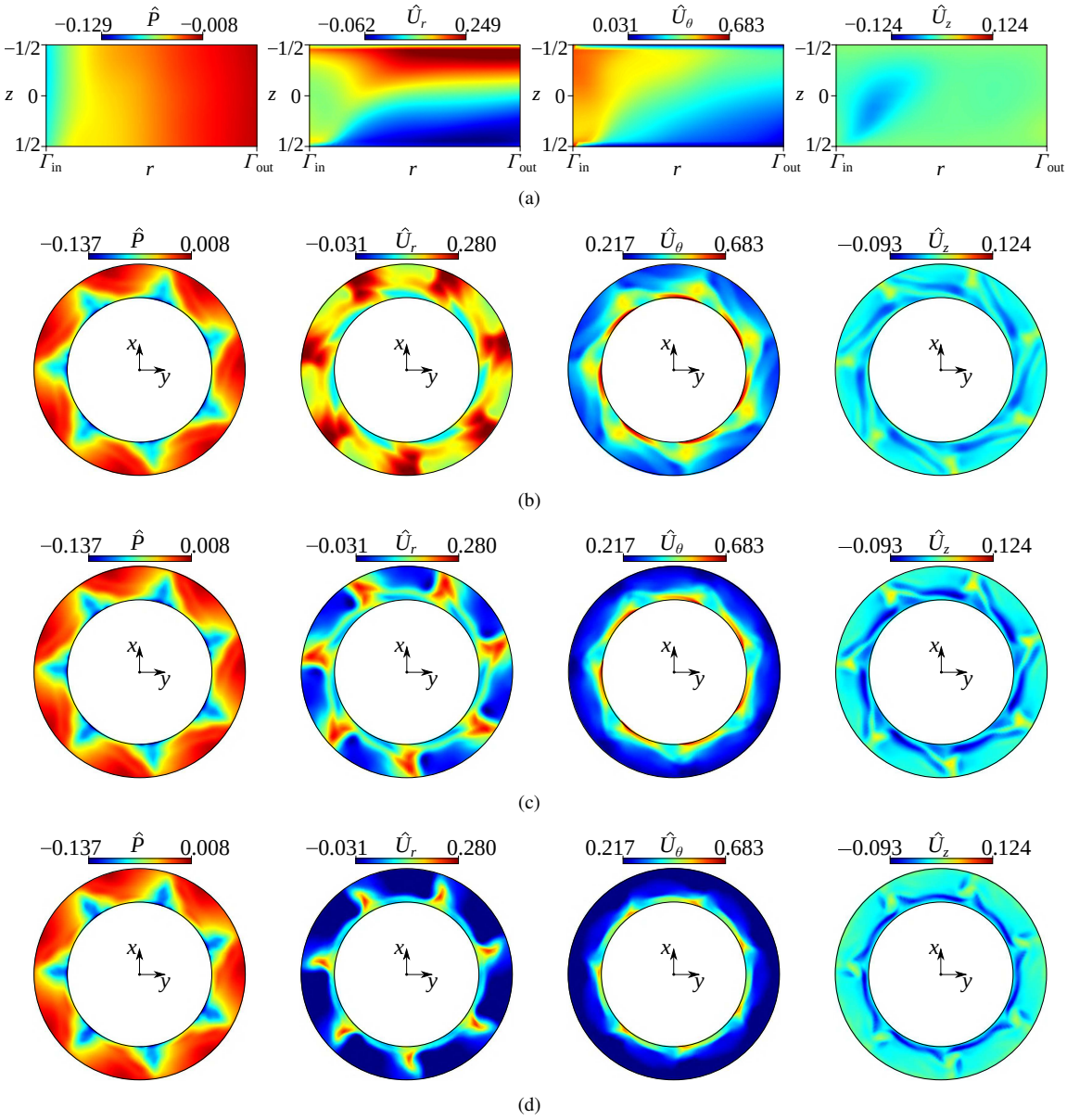

FIG. 10. Colour Maps (from left to the right side) of instantaneous static pressure, radial velocity, tangential velocity, and axial velocity distribution at (a) the meridian section of the pump (azimuth arithmetic average values), (b) shroud side, (c) mid-height and (d) hub side of the diffuser at the design flow rate Q/Q_d = 1.00 of the zero-leakage case obtained by the URANS simulation.

enables the detection of rotating phenomena[31,32] and gives their characteristics in terms of a number of cells and propagation velocity. The cross-power spectrum of the zero-leakage case is shown in fig. 11(a). The blade-passing-to-impeller-frequency ratio $f_{blade}/f_{imp} = 7$ can be observed very clearly as expected, where f_{blade} and f_{imp} denote the blade passing and the impeller frequency, respectively. Another frequency is detected corresponding to $f/f_{imp} = 1.543$. As this frequency is not compatible with any of the super-/sub-harmonics of the impeller or blade passing frequencies, respectively, the flow was simulated for one additional impeller revolution in order to inspect the origin of such an unexpected frequency. The video of the corresponding velocity magnitude is given as supplementary material. By visual inspection of the video, we figured out that the frequency $\tilde{f}/f_{imp} = 1.543$ is compatible with a rotating pattern having a propagation velocity that is approximately estimated to be about five times slower than the impeller velocity. Moreover, the amplitude of the rotating pattern is also consistent with the amplitude of the cross-power spectra of the two probe signals in the vaneless diffuser.

A more quantitative analysis was therefore required to further clarify the origin of the incommensurate frequencies in the FFT. As the highest amplitude of the cross-power spectrum is produced by such an unexpected rotating pattern, the rotational velocity can be quantified by $\tilde{f}/f_{imp} = 1.543$, corresponding to $\tilde{\omega}/\omega_{imp} = 0.22$. This propagation velocity is

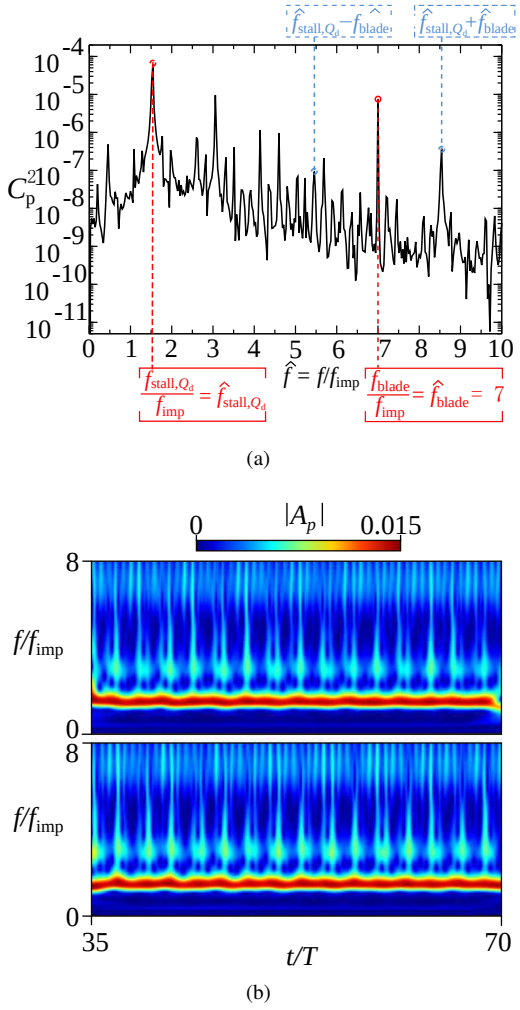

FIG. 11. (a) Fourier and (b) wavelet analysis of the URANS simulation of the zero-leakage case at the design flow rate Q/Q_{d} =1.00.

therefore consistent with the about-five-times-slower pattern rotating around the blade wake observed in the video. The slow rotating pattern is moreover consistent with the rotating instability reported by Ljevar, de Lange, and van Steenhoven [10], who investigated the core flow in a vaneless diffuser varying the blade jet-to-wake intensity, the number of blades and the outlet-to-inlet diffuser radius ratio. By employing a two-dimensional model, hence neglecting the boundary layers on the hub and the shroud, they report a rotating instability whose mode, propagation speed and critical conditions depend on the three parameters of their study. For $R_4/R_3 = 1.48$ corresponding to our diffuser their data lead to either a 6- or a 7-periodic pattern for the rotating instability, which is consistent with our observations. Moreover, the propagation velocity of their rotating stall is about $\omega_{\mathrm{stall},Q_{\mathrm{d}}}/\omega_{\mathrm{imp}} = 0.3$, which is of the same order of our $\tilde{\omega}/\omega_{\mathrm{imp}} = 0.22$ even if slightly faster. This can be explained by considering that in our three-dimensional flow the boundary layer tends to oppose resistance to the rotating stall at nominal flow conditions, resulting in a slowed-down rotating pattern. Further considering that our core flow has a blade jet-to-wake angle smaller than the critical angle predicted by Ljevar, de Lange, and van Steenhoven [10] below which the rotating stall occurs, we infer that the rotating pattern producing the frequency $\tilde{f}/f_{\mathrm{imp}} = f_{\mathrm{stall},Q_{\mathrm{d}}}/f_{\mathrm{imp}} = 1.543$ is indeed a rotating instability.

The other peaks of the power spectrum corresponding to sub-/super harmonics of the fundamental frequencies or nonlinear interactions among them. Further quantification of this complex flow topology is investigated by two independent wavelet analyses carried out for the two probe signals used for the cross-power spectrum (see fig. 11(b)). Both wavelet analyses reveal extra details. In fact, in addition to the blade passing $f_{\mathrm{blade}}/f_{\mathrm{imp}} = 7$ and the rotating instability frequency $f_{\mathrm{stall},Q_{\mathrm{d}}}/f_{imp} = 1.543$ detected by Fourier analysis, we also observe an intermittent phenomenon whose frequency of about $f/f_{\mathrm{imp}} \approx 3$. Because of the nonlinear interactions between the rotating stall and the shear layer of the impeller discharge, a pulsating high-order effect emerges at the cusps of the slow rotating flow pattern. This is depicted in the four snapshots shown in fig. 12 for one pulsating frequency, i.e. for $t/T \in [70.18,\ 70.29]$. The robustness of such a pulsating pattern is demonstrated by the identification of the corresponding wavelet features for more than the last 40 revolutions of the impeller and the corresponding breathing pattern is well depicted in the wavelet analysis (fig. 11(b)) for the last 35 revolutions.

To further quantify the number of stall cells and visualize their topology, the unsteady flow field associated with the rotating instability is phase-averaged. The corresponding color maps are produced with 120-time steps of the last revolution for two rotating reference frames. Figure 13(a) shows the averaged flow field in a reference frame rotating with the impeller. A mode-7 jet-wake flow rotating with the impeller can be observed near the diffuser inlet as expected. Besides, fig. 13(b) shows the averaged flow field in a reference frame rotating with the propagation velocity of the instability. Another 7-periodic pattern can be observed, consistently with the prediction of Ljevar, de Lange, and van Steenhoven [10]. Therefore, two different kinds of azimuthally-traveling patterns exist at the same time at the design flow rate $Q = Q_{\mathrm{d}}$ for the zero-leakage case. The first one is expected to correspond to the classical jet-wake pattern, while the second one is consistent with the literature and found for the first time in our pump. Moreover, subtracting the phase-averaged jet-wake pattern from the total flow, fig. 13(c) demonstrates that the pulsating mode observed in fig. 11(c) is azimuthally stationary in a reference frame rotating with $\omega_{\mathrm{stall},Q_{\mathrm{d}}}$, it is produced near the boundary of the jet wake and advected downstream towards the outlet of the diffuser. To the best of the authors' knowledge, this secondary instability has never been reported in the literature.

The leakage between the impeller and the diffuser changes the inflow conditions of the vaneless diffuser and a significant influence on the corresponding bulk flow is therefore expected. The effect of leakage flow on the diffuser at design flow rate $Q = Q_{\mathrm{d}}$ is therefore analyzed in this section. Considering the azimuthally-averaged color maps at the meridian

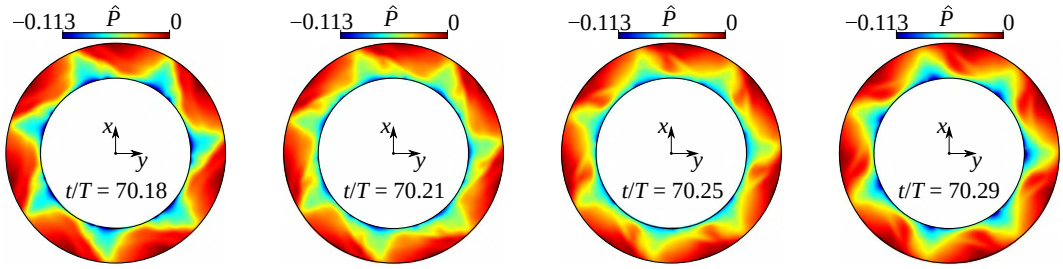

FIG. 12. Snapshots of the static pressure color map of the zero-leakage case at the design flow rate $Q/Q_{\mathrm{d}} = 1.00$ at different calculation time $t/T \in [70.18,\ 70.29]$

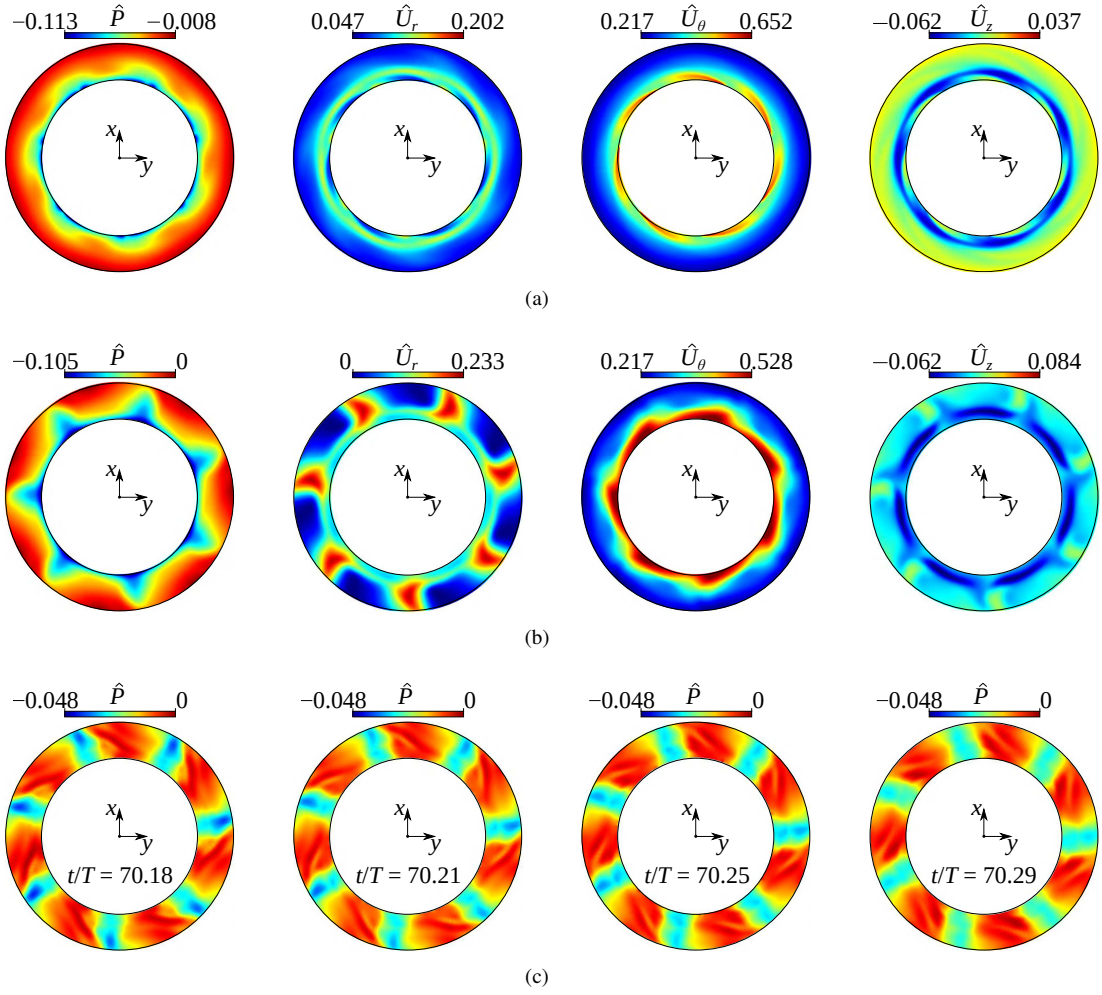

FIG. 13. Phase averaged color maps of the static pressure, radial velocity, tangential velocity and axial velocity with (a) the impeller rotating velocity ω_{imp}, and (b) the instability propagation velocity $\omega_{\mathrm{stall},Q_{\mathrm{d}}}$ of the zero-leakage case at design condition $Q/Q_{\mathrm{d}} = 1.00$,and (c) the snapshots of the static pressure field subtracted the phase-averaged flow with ω_{imp} for $t/T \in [70.18,\ 70.29]$.

section and the instantaneous color maps at the mid-height section in the vaneless diffuser for our three numerical configurations. For the zero-leakage case (see Appendix C (a)), the flow field is most significantly influenced by the impeller jet wake and the emerging of the rotating stall described in Sec. IV C 1. For the negative-leakage case (see Appendix C (b)), the flow rate in the diffuser does not change significantly, which means that the inflow conditions at the diffuser resemble the ones observed for the zero-leakage case. The flow field in the negative-leakage case is therefore found to be similar to the corresponding one for the zero-leakage case, where 7-periodic patterns (both from the impeller jet wake and from the rotating stall) can clearly be identified. For the positive-leakage case (see Appendix C (c)), on the other hand, the leak-

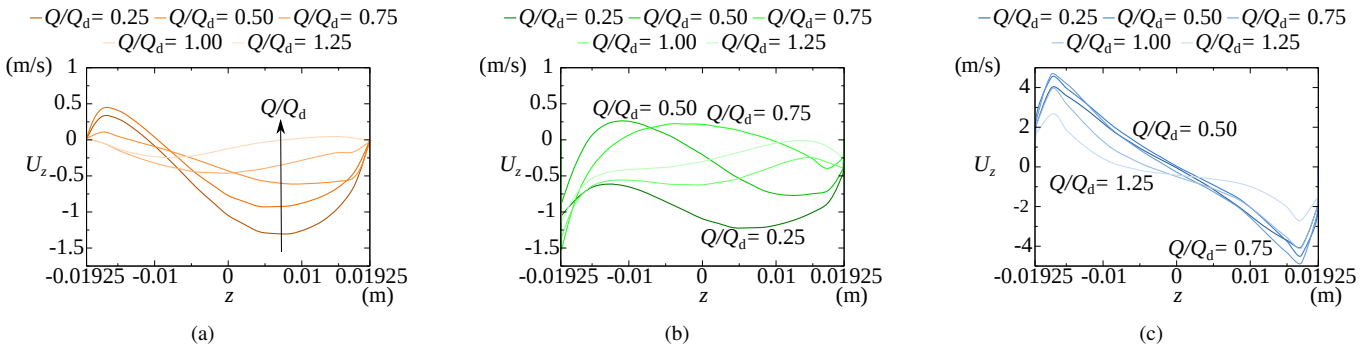

FIG. 14. Axial velocity profiles at the diffuser inlet of (a) the zero-leakage case, (b) the negative-leakage case, and (c) the positive-leakage case.

age flow entering the diffuser from the hub and the shroud side is stronger and has a stabilizing effect on the periodic pattern of the jet wake as the effective flow angle increased (see Ljevar, de Lange, and van Steenhoven [10]). This leads to a more symmetrical azimuthally-averaged velocity distribution in z and to a more complicated and less symmetrical core flow at the midplane. The increased significance of the leakage flow for the positive-leakage case is further confirmed by fig. 14 that depicts the axial velocity profile at the diffuser inlet for all three pump configurations. The zero- and negative-leakage cases have very similar axial velocity profiles, whose maximum absolute values at the design flow rate are about 2% to 5% the maximum tangential velocity of the jet wake. On the other hand, the positive-leakage case has an axial velocity whose maximum values are about 20% of $\max(U_\theta)$. This explains how the far more significant values of U_z for the positive-leakage case at the diffuser inlet are capable of remarkably perturbing the blade's wake. As the jet-wake flow at the diffuser entrained air through the radial gap (positive-leakage flow), the critical conditions needed to trigger the 7-periodic rotating stall are not met. This explains why the 7-periodic pattern far from the diffuser inlet is not observed in the instantaneous flow fields of the core flow for the positive-leakage case. In fact, the 7-periodic pattern due to the rotating stall detected by visual inspection of the core-flow videos for the zero- and negative-leakage cases can no longer be found in the positive-leakage case.

A more quantitative analysis was therefore carried out to further substantiate the interpretation of the qualitative evidence derived by visual inspection of the core-flow videos. Figure 15 presents the comparison of the FFT and wavelet analysis for the URANS simulations and the experiments at the design flow rate $Q = Q_\mathrm{d}$. In agreement with the qualitative inspection, a rotating instability is signaled for zero- and negative-leakage case (see figs. 15(a,b)). For the negative-leakage case (fig. 15(b)), the frequency components are similar to the ones detected for the zero-leakage case. However, the secondary instability leading to a pulsating flow traveling with the primary rotating stall instability is not as clear in the wavelet analysis as it was for the zero-leakage case. This leads to conclude that even a small leakage flow may significantly impact the secondary instability. On the other hand, such a small leakage does not remarkably affect the primary instability. This is confirmed by tab. III that reports the primary rotating instability characteristics for all our cases. The propagation velocity $\omega_{\mathrm{stall},Q_\mathrm{d}}/\omega_\mathrm{imp} = 0.22$ measured for the numerical simulations in the zero-leakage case gets only slightly modified by the negative-leakage, passing to $\omega_{\mathrm{stall},Q_\mathrm{d}}/\omega_\mathrm{imp} = 0.224$. For the positive-leakage case (fig. 15(c)) only the blade passing frequency can be observed. This is in good agreement with experiments (fig. 15(d)) as they are produced in a similar positive-leakage configuration. As anticipated by inspecting the core-flow videos, no rotating stall frequency is found in the Fourier spectrum of the positive-leakage cases (URANS simulations, fig. 15(c), and experiments, fig. 15(d)).

Figure 16 shows the comparison of the phase-averaged flow field in a reference frame rotating with the impeller at ω_imp. The color maps for the three different geometries show that the 7-periodic jet-wake pattern near the diffuser inlet always exists in the phase-average flow, even for the positive-leakage flow whose instantaneous flow field did not clearly show the jet-wake periodic pattern. The jet-wake pattern found by phase averaging is consistent with the Fourier analysis thanks to which the blade-passing frequency could be identified in the frequency spectrum. As the propagation velocity of the rotating stall does not significantly change with the leakage flow, fig. 17 shows the comparison of the phase-averaged flow field in a reference frame rotating with $\omega_{\mathrm{stall},Q_\mathrm{d}} = 0.22\omega_\mathrm{imp}$. For the zero- and the negative-leakage cases, the corresponding 7-periodic pattern of the rotating stall is found far from the diffuser inlet. On the other hand, for the positive-leakage case, this kind of instability does not occur, hence no major non-zero modal coherence is found in the respective phase-average core flow rotating with with $\omega_{\mathrm{stall},Q_\mathrm{d}} = 0.22\omega_\mathrm{imp}$. This observation is consistent with the corresponding FFT and wavelet analysis.

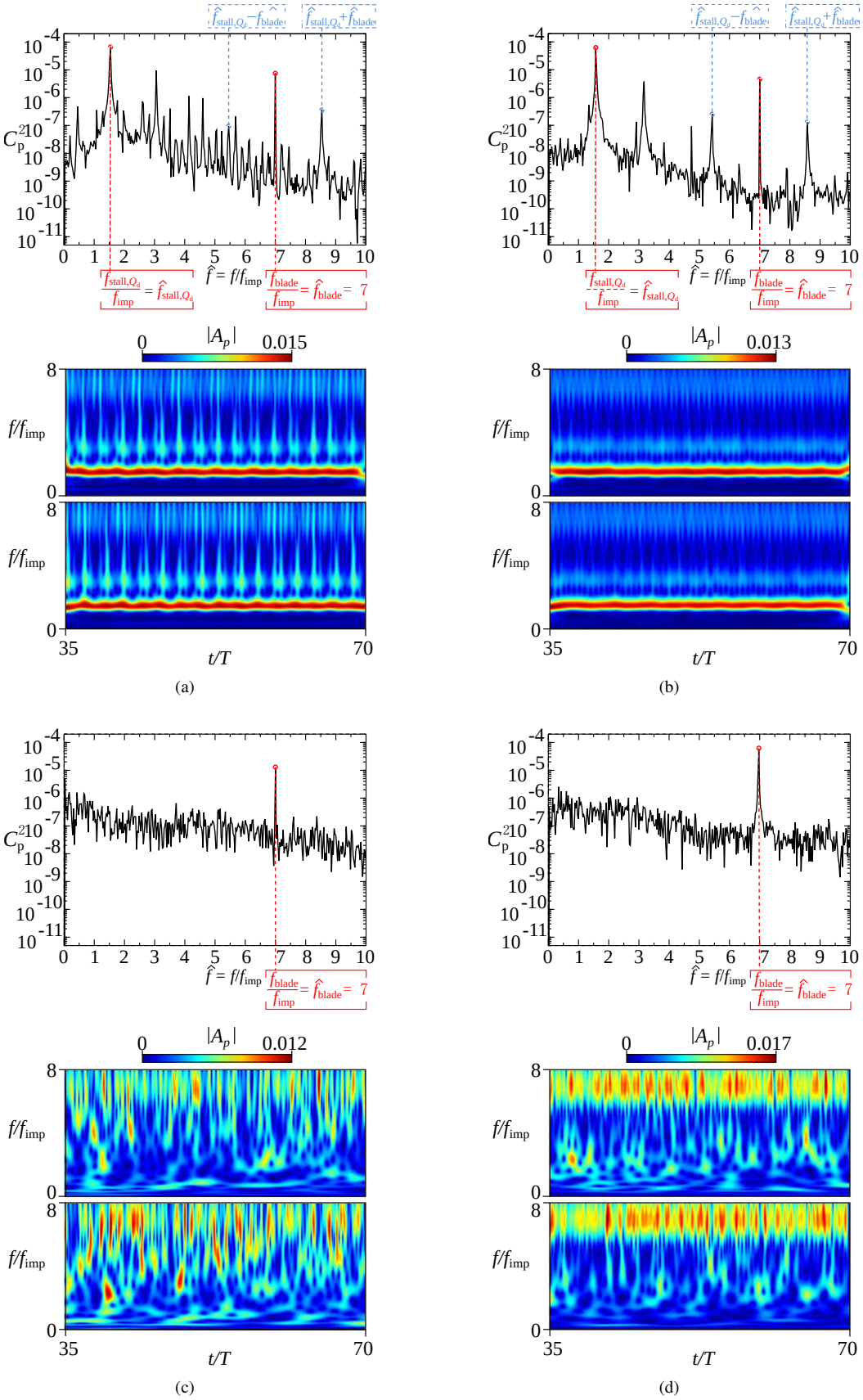

FIG. 15. Fourier and wavelet analysis of the URANS simulation for (a) the zero-leakage case, (b) the negative-leakage case, and (c) the positive-leakage case, and of (d) the experiment, at the design flow rate $Q/Q_{\mathrm{d}} = 1.00$.

TABLE III. Propagation velocity of the rotating instability obtained by the cross-correlation analysis at the design flow rate Q/Q_{d} = 1.00.

Case	Zero-leakage (URANS)	Negative-leakage (URANS)	Positive-leakage (URANS&Exp)
$f_{\mathrm{stall},Q_{\mathrm{d}}}/f_{\mathrm{imp}}$	1.543	1.571	/
$\omega_{\mathrm{stall},Q_{\mathrm{d}}}/\omega_{\mathrm{imp}}$	0.220	0.224	/

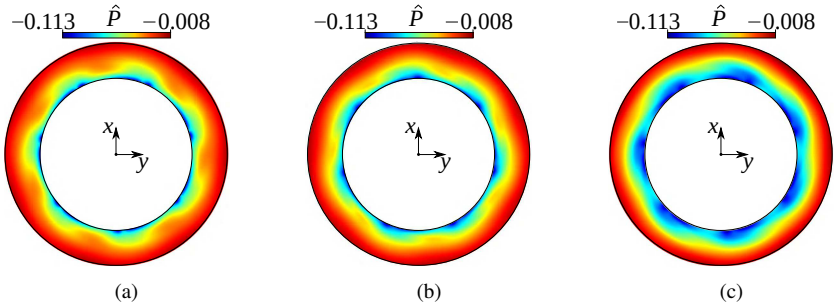

FIG. 16. Color maps of phase averaged static pressure at the mid-height of the diffuser based on the impeller rotating speed ω_{imp} at the design flow rate $Q/Q_{\mathrm{d}} = 1.00$ for (a) the zero-leakage case, (b) the negative-leakage case and (c) the positive-leakage case.

D. Effect of the flow rate on the flow field for the zero-leakage case

1. *Flow field analysis*

To understand how the flow in the vaneless diffuser is affected by the flow rate Q, we vary the inflow conditions at the inlet pipe ranging from $Q/Q_{\mathrm{d}} = 1.25$ down to $Q/Q_{\mathrm{d}} = 0.25$. The azimuthally-averaged color maps at the meridian section (fig. 18) and the instantaneous color maps of the mid-height of the diffuser (fig. 19) are depicted for five flow rates $Q/Q_{\mathrm{d}} \in [0.25,\ 1.25]$ with $\Delta Q/Q_{\mathrm{d}} = 0.25$, where ΔQ is the increment in flow rate at the inlet pipe. The static pressure and the three velocity components are also analyzed separately to better distinguish the flow structures within the velocity field.

Looking at fig. 18(a), the plot of the radial velocity at the largest flow rate ($Q/Q_{\mathrm{d}} = 1.25$) indicates that the bulk flow in the diffuser passage is dominated by inviscid effects. Indeed, it well resembles an Euler-flow solution except for the azimuthally-averaged reverse flow region (blue area in U_r). Under the influence of the non-uniform swirling inflow coming from the rotating impeller, the incoming jet forces the blockage of the vortexes, which are pushed towards the diffuser outlet and confined near the walls. Flow separation and reverse flow occur up to a large extent near the outlet of the hub (not shown). The color maps at the mid-height of the diffuser (fig. 19(a)) show that the velocity and the pressure are regularly distributed, and the main flow streamline is a nearly logarithmic spiral curve. Besides, the jet-wake pattern can be clearly observed in the color map of the static pressure distribution with seven high-pressure peaks. In these flow conditions, the increase of the mean flow angle is responsible for the stabilization of the flow (see fig. 9(a) of Ljevar, de Lange, and van Steenhoven [10]) and no jet-wake-induced rotating instability was observed.

As the flow rate decreases down to the design flow rate, i.e. for $Q/Q_{\mathrm{d}} = 1.00$, fig. 18(b) shows that the reverse flow region becomes surface-filling over the hub (see blue zone in U_r, fig. 18(b)), occupying almost half of the diffuser passage in $z-$direction. We recall that a core-flow rotating instability has been identified for $Q/Q_{\mathrm{d}} = 1.00$ design flow rate (see Sec. IV C 1). The massive reverse flow is due to the significant pressure and velocity magnitude of the rotating stall at design flow rate. In fact, the same mean flow separation is observed for the negative-leakage case, where the rotating stall has been identified (see fig. C(b)). On the other hand, no rotating stall instability has been found for the positive-leakage case at design flow rate and the reverse flow region is almost absent in the azimuthally-average flow (see fig. C(b)). Consistently, we further recall that no massive flow separation has been observed for $Q/Q_{\mathrm{d}} = 1.25$ in the zero-leakage flow (see fig. 19(a)) as the rotating stall does not occur. This points towards a clear indication that the rotating stall phenomenon described in Sec. IV C 1 is responsible for the distinct massive azimuthally-averaged reverse flow region observed in the diffuser. This is consistent with the observations of Ljevar, de Lange, and van Steenhoven [10] (see figs. 3 and 4 of their paper).

As the flow rate further decreases to $Q/Q_{\mathrm{d}} = 0.75$, fig. 18(c) shows that the influence of the asymmetrically distributed inflow velocity weakened. This is consistent with the interpretation of the rotating stall being responsible of the azimuthally-averaged reverse flow region. In fact, for $Q/Q_{\mathrm{d}} = 0.75$ no rotating stall is observed as the decrease of the jet-wake intensity led to a stabilization of the flow. This is demonstrated by figure fig. 19(c), whose color maps at the mid-height of the diffuser show that the 7-periodic rotating instability pattern disappeared (cf. with the rotating stall observed at the design flow rate $Q/Q_{\mathrm{d}} = 1.00$, fig. 19(b)). Owing to the mass conservation law and the friction loss, the radial velocity tends to

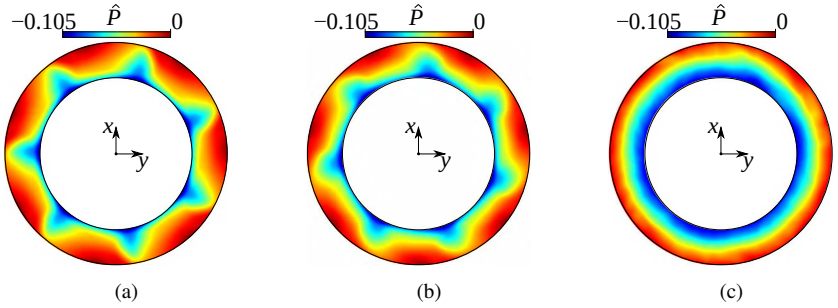

FIG. 17. Color maps of phase averaged static pressure at the mid-height of the diffuser based on the instability propagation speed ω_{ins} at the design flow rate $Q/Q_{\mathrm{d}} = 1.00$ for (a) the zero-leakage case, (b) the negative-leakage case and (c) the positive-leakage case.

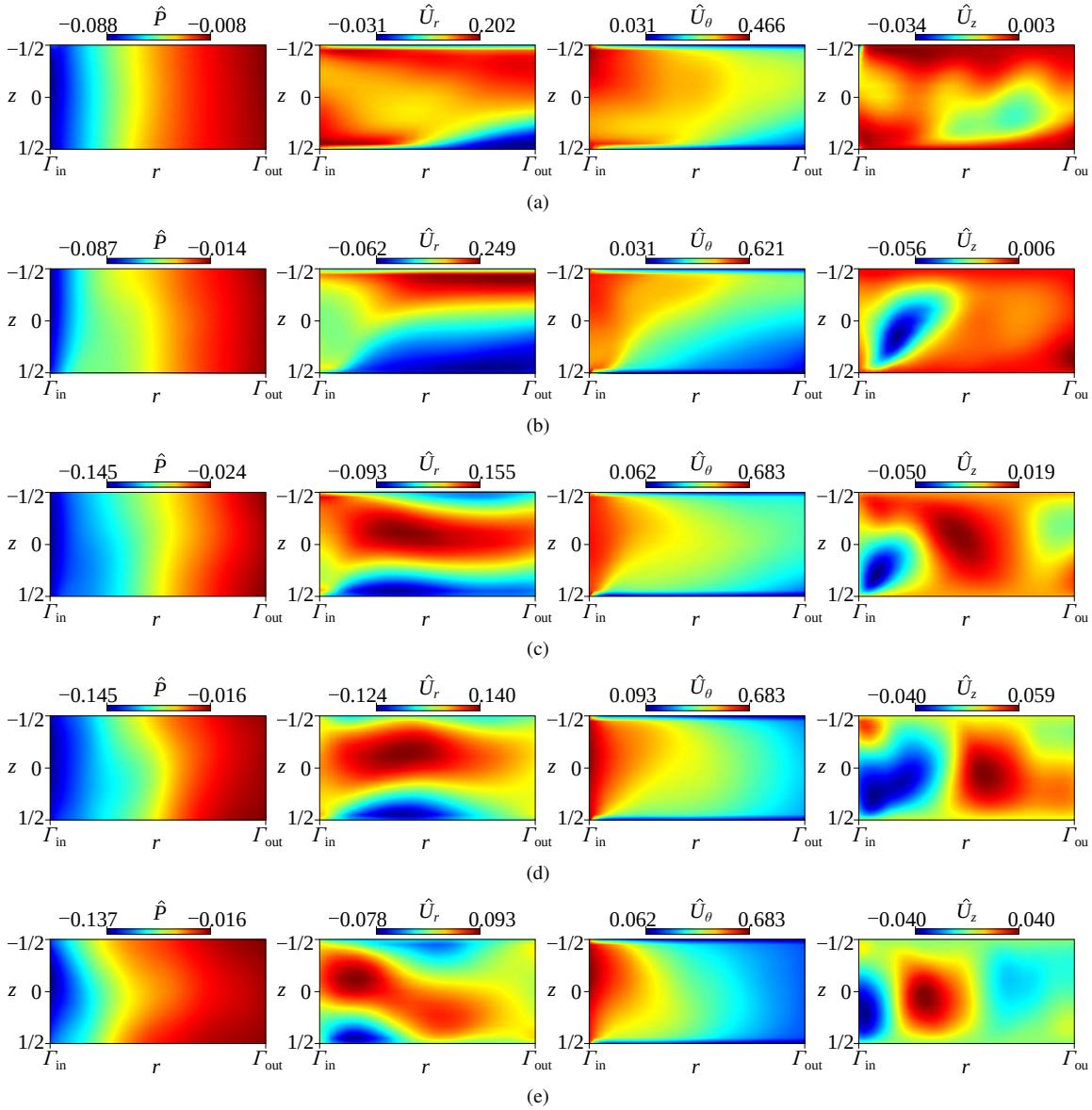

FIG. 18. Color maps of the azimuth averaged instantaneous static pressure, radial velocity, tangential velocity, and axial velocity at the meridian section of the diffuser at the flow rate (a) $Q/Q_{\mathrm{d}} = 1.25$, (b) $Q_d = 1$, (c) $Q/Q_{\mathrm{d}} = 0.75$, (d) $Q/Q_{\mathrm{d}} = 0.50$, and (e) $Q/Q_{\mathrm{d}} = 0.25$.

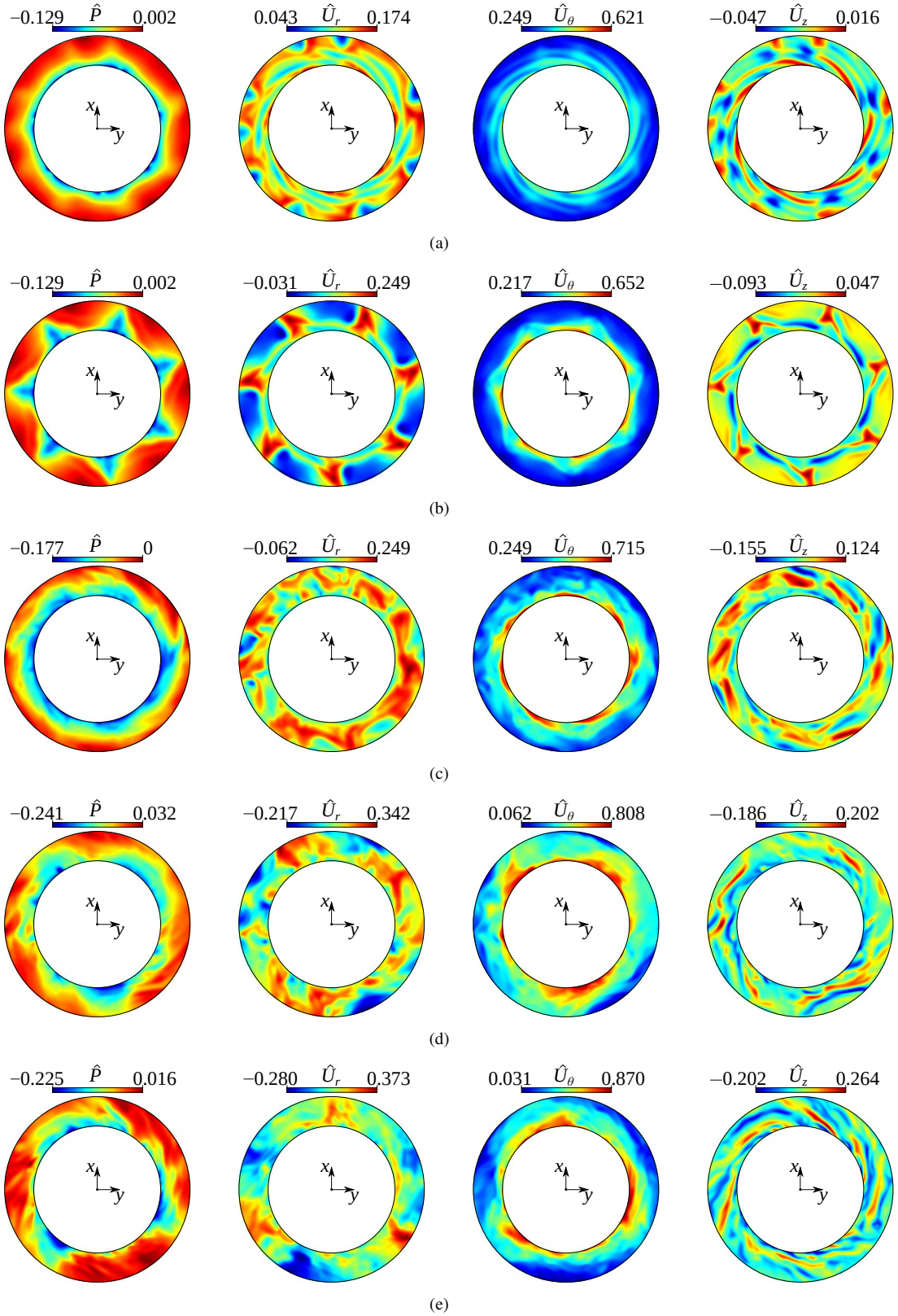

FIG. 19. Color maps of instantaneous static pressure, radial velocity, tangential velocity, and axial velocity at the mid-height of the diffuser at the flow rate (a) $Q/Q_{\mathrm{d}} = 1.25$, (b) Q_d, (c) $Q/Q_{\mathrm{d}} = 0.75$, (d) $Q/Q_{\mathrm{d}} = 0.50$, and (e) $Q/Q_{\mathrm{d}} = 0.25$.

decrease along the diffuser radius, although it increases near the inlet under the effect of the increased boundary layer thickness. Azimuthally-averaged flow separation and reverse flow regions can be observed near the shroud and hub walls.

Upon a decrease of the flow rate down to $Q/Q_{\mathrm{d}} = 0.5$, a stronger flow separation occurs especially near the diffuser inlet of the hub side. Moreover, the mean flow inside the vaneless diffuser becomes more skewed (see fig. 18(d)) and several backflow regions can be observed near the diffuser outlet (see fig. 19(d)). Three rotating stall cells are apparent, especially considering the pressure and the azimuthal flow fields at mid-plane (see leftmost and second-right panels in fig. 19(d)). This rotating instability has previously been reported by several authors who investigated it numerically and experimentally[11,12,30]. The associated azimuthally-averaged reverse flow regions are not as evident as for the rotating stall at design flow rate (cf figs. 18(b) and (d)). We speculate that this is due to the weaker energy transfer from the jet-wake to the rotating stall upon a decrease of the flow rate.

For the lowest flow rate $Q/Q_{\mathrm{d}} = 0.25$, fig. 18(e) shows that the high-radial velocity region moved towards the diffuser inlet and the mean flow near the diffuser inlet tends to exhibit a clearer S-shape with reverse flow near the shroud and hub walls close to the vaneless diffuser inlet. As the flow rate decreased, the rotating stall became more supercritical and the mode-3 patter can more clearly be distinguished. In fact, three rotating stall cells composed of a core of outward radial velocity followed by a zone of inward radial velocity are quite well identifiable in the color maps at the mid-height of the diffuser (see fig. 19(e)). The core flow changes are associated to the wake-jets coming out of the impeller discharge. Moreover, the streamlines inside the vaneless diffuser are strongly distorted and are far from the the ideal logarithmic spiral curve, especially in the area corresponding to the low-velocity regions. This same observations are reported in the literature and are in significant agreement with the PIV visualizations performed for the same type of vaneless diffusers[12].

E. Rotating stall at the smallest flow rates

1. *Instability mechanism*

At large-enough flow rates, if the rotating stall does not occur (see e.g. $Q/Q_{\mathrm{d}} = 1.25$ and $Q/Q_{\mathrm{d}} = 0.75$ for the zero-leakage case), the core flow away from the walls experiences a quasi two-dimensional development from the diffuser inlet to the outlet and the flow streamlines follow a nearly logarithmic spiral curve. Upon a decrease of the flow rate, the rotating stall at low design flow rates can therefore be studied as a core-flow instability if the boundary layers along the shroud and the hub of the vaneless diffuser are thin. This is the case of so-called "wide" diffusers. We stress that the two-dimensional core instability argument holds if the turbulent boundary layers on the diffuser walls do not exhibit significant three-dimensional features leading to flow separations that may occur owing to the high adverse pressure gradient produced by the radial increase of the diffuser section in the $(\phi, z)-$plane when moving from inlet to outlet.

Under the hypothesis of a two-dimensional core-flow mechanism, we employ the analytical model of Tsujimoto, Yoshida, and Mori [8] in order to characterize the components of the energy budget leading to a transfer of energy from the two-dimensional basic state to the two-dimensional most-dangerous infinitesimal perturbation. This linear stability analysis has successfully predicted the mode-3 instability observed in Heng, Dazin, and Ouarzazi [9], Heng *et al.* [29,30] (see fig. 19(d–e)) and it will further help to clarify the origin of the rotating stall at low flow rates. We however anticipate that the corresponding low-flow-rate rotating stall is somehow simpler than the rotating stall observed at the design flow rate for the zero- and the negative-leakage flow. In fact, in the latter case, the rotating instability is strongly affected by the non-homogeneous forcing in $\theta-$direction. On the contrary, at low flow rates, the mechanism proposed by Tsujimoto, Yoshida, and Mori [8] relies exclusively on the skewness of the diffuser inflow and does not involve any inhomogeneous forcing in θ. In fact, the analytical model of Tsujimoto, Yoshida, and Mori [8] considers an infinite number of blades, hence a uniform inflow in θ which is solely characterized by its jet-wake angle.

For the model of Tsujimoto, Yoshida, and Mori [8], several assumptions were made:

- a two-dimensional incompressible and inviscid flow is considered,
- the boundary conditions are axisymmetric, i.e. uniform static pressure at diffuser outlet and imposed velocity magnitude and flow angle at inlet,
- the flow field is described as a superposition of a steady basic state and an infinitesimal rotating perturbation determined by linear stability analysis.

Within such assumptions, the basic state streamlines in the vaneless diffuser are logarithmic spirals from diffuser inlet to outlet. Hence, the basic state solution is essentially one-dimensional as it is invariant to rotation along the logarithmic spiral. Non-dimensionalizing by using the quantities R_3, $(2\pi R_3^2)/Q$, $Q/2\pi R_3$, and $\rho Q^2/(2\pi R_3)^2$ to scale length, time, velocity, and pressure, respectively, the basic state velocity $\vec{U}_0 = (U_{0,r}, U_{0,\theta})$ and pressure P_0 read:

$$\begin{aligned} U_{0,r} &= \frac{1}{r}, \\ U_{0,\theta} &= \frac{\mu}{r}, \\ P_0 &= -\frac{1}{2}\left(1+\mu^2\right)\left(\frac{1}{r^2}+\frac{1}{R^2}\right), \end{aligned} \tag{13}$$

where $\mu = U_{0,\theta}/U_{0,r}|_{r=1}$ and $1 < r < R = R_4/R_3$. We further remark that such a basic state is irrotational, i.e. $\nabla \times \vec{U}_0 = 0$. Carrying out a linear stability analysis, the total flow in the vaneless diffuser results from the sum of the basic state and

the infinitesimal perturbation (prime sign):

$$\begin{aligned} U_r &= U_{0,r}(r) + u'_r(r,\theta,t), \\ U_\theta &= U_{0,\theta}(r) + u'_\theta(r,\theta,t), \\ P &= P_0(r) + p'(r,\theta,t), \end{aligned} \tag{14}$$

where $\vec{u}' \ll \vec{U}_0$ and $p' \ll P_0$. As the basic state is steady and homogeneous in θ, the ansatz for the infinitesimal perturbation is:

$$\left\{u'_r, u'_\theta, p'\right\}(r,\theta,t) = \left\{\tilde{u}_r, \tilde{u}_\theta, \tilde{p}\right\}(r) e^{i\xi t - im\theta}, \tag{15}$$

where m is the wavenumber, i.e. the number of rotating stall cells. The complex frequency ξ could be divided in a real χ and complex σ part, i.e. $\xi = \chi - i\sigma$. The real part χ is the angular frequency, while σ is the growth rate of the instability. The flow is unstable (stable) when $\sigma > 0$ ($\sigma < 0$) and the mathematical problem is closed by enforcing the boundary conditions proposed by Tsujimoto, Yoshida, and Mori [8]:

$$r = 1 : \tilde{u}_r = \tilde{u}_\theta = 0; \qquad r = R : \tilde{p} = 0. \tag{16}$$

The neutral stability modes are then obtained by setting $\sigma = 0$, fixing m, and following the algorithm proposed by Heng, Dazin, and Ouarzazi [9], which makes use of a shooting method for approaching the analytical solution by successive iterations.

An a posteriori analysis of the kinetic energy transferred between the basic state and the critical mode is here employed to identify the physical mechanisms leading to the flow instability and to validate the overall energy conservation of our neutral mode. To that end, we numerically evaluate all terms of the inviscid Reynolds-Orr-equation

$$\frac{dE^{kin}}{dt} = \sum_{k=1}^{4} \int_V I'_k dV + K^{out}, \tag{17}$$

where E_{kin} is the total kinetic energy, I'_k are the kinetic energy densities resulting from the non-linear term of the incompressible Euler equations, and

$$K^{\text{out}} = -\frac{1}{2} \int_S U_{0,r} {u'_r}^2 S^{\text{out}}, \tag{18}$$

is the transport of perturbation energy through the outlet surface S^{out}. Since $\tilde{u} = 0$ at the inlet, no perturbation energy is advected into the system from upstream. Moreover, the work done by pressure forces does not contribute to the energy budget as we assume that the pressure perturbations vanish at the outlet (i.e. $\tilde{p} = 0$ at $r = R$). To ease the interpretation of the energy budget, the local energy production rates are decomposed along the streamline coordinates of the basic state, i.e.

$$\vec{u}' = \vec{u}'_{\parallel} + \vec{u}'_{\perp}, \tag{19}$$

where $\vec{u}'_{\parallel}$ is the perturbation component projected along the basic state streamlines, while $\vec{u}'_{\perp} = \vec{u}' - \vec{u}'_{\parallel}$ is the normal component. The corresponding energy density terms I'_k read:

$$\begin{aligned} \sum_{k=1}^{4} I'_k = -[&\vec{u}'_{\perp} \cdot (\vec{u}'_{\perp} \cdot \nabla \vec{U}_0) + \vec{u}'_{\parallel} \cdot (\vec{u}'_{\perp} \cdot \nabla \vec{U}_0) \\ &+ \vec{u}'_{\perp} \cdot (\vec{u}'_{\parallel} \cdot \nabla \vec{U}_0) + \vec{u}'_{\parallel} \cdot (\vec{u}'_{\parallel} \cdot \nabla \vec{U}_0)], \end{aligned} \tag{20}$$

where k numbers all terms on the right-hand side consecutively. The sign of the integrands I'_k determine whether the local energy transfer acts as a destabilizing (positive) or a stabilizing (negative) contribution. If the rate of change of the kinetic energy $\frac{dE^{kin}}{dt}$ is positive, the basic flow is unstable, and vice versa. Hence the energy budget is also used to verify the linear stability results, because the rate of change of the kinetic energy must vanish for the neutral modes, i.e.

$$\frac{dE^{kin}}{dt}|_{\sigma=0} = 0. \tag{21}$$

In our computations, such a condition is verified at the 5-th digit, hence we can consider our computation of the neutral mode validated.

The scalar field of the energy production rates in the bulk are given in fig. 20 for the critical modes, i.e. for $m = 3$. As they result from the energy density of the perturbation (hence they involve the square of the perturbation velocity), their wavenumber is twice the perturbation m. Figure 20 clearly identifies a mode-3 critical perturbation, in agreement with what already reported in the mid-height colormaps for our URANS simulations. Moreover, the spiralling character of the I'_k fields is characteristic of a rotating instability, hence of rotating stall. We anticipate however that we find that the critical propagation velocity obtained by the model of Tsujimoto, Yoshida, and Mori [8], $\chi = 0.289$ is larger compared to our URANS simulations. This is expected because the two-dimensional model of Tsujimoto does not account for the resistance due to the hub and shroud wall.

To complement the qualitative interpretation done so far relying on the scalar fields of I'_k, fig. 21 reports the total energy budget. Our results show that $\int_V I'_2 dV$, $\int_V I'_3 dV$ and $\int_V I'_4 dV$ are contributing to the destabilization of the basic state, with $\int_V I'_4 dV$ being slightly dominant in magnitude. On the other hand, $\int_V I'_1 dV$ has a minor stabilizing effect, while most of the energy produced by $\int_V I'_2 dV$, $\int_V I'_3 dV$ and $\int_V I'_4 dV$ is transported outside of the diffuser leading to a high-magnitude, negative K^{out}. There are, therefore, two mechanisms contributing to the instability of the diffuser basic state:

1. The lift-up mechanism, that describes how the basic flow momentum is transported in normal direction to the basic state streamlines by $\vec{u}'_{\perp} \cdot \nabla \vec{U}_0$ and feeds back on the parallel component of the critical perturbation $\vec{u}'_{\parallel}$. This is represented by the $I'_2 = -\vec{u}'_{\parallel} \cdot (\vec{u}'_{\perp} \cdot \nabla \vec{U}_0)$, which in our flow coincides with the I'_3, as also depicted in fig. 20.

2. The strong streamwise deceleration due to the radial increase of the diffuser cross section. This is always a destabilizing effect because I'_4 has a quadratic term in $\vec{u}_{\parallel}$, hence its sign is solely determined by the gradient of the basic flow momentum transported along the streamlines. A decrease of basic state momentum leads to a positive contribution of $I'_4 = -\vec{u}'_{\parallel} \cdot (\vec{u}'_{\parallel} \cdot \nabla \vec{U}_0)$, therefore to a transfer of energy from the basic state to the perturbation.

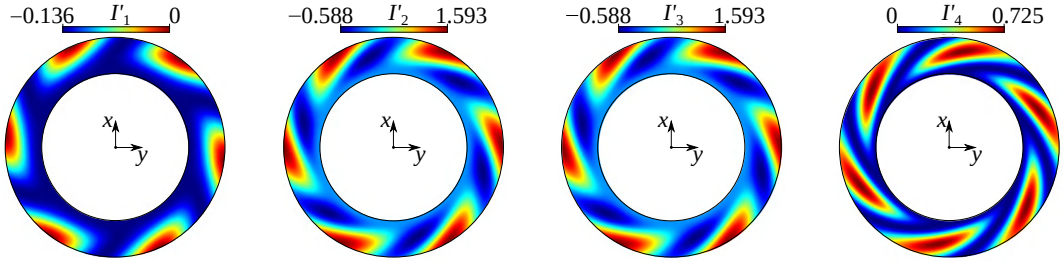

FIG. 20. Color maps of normalized local energy-transfer terms.

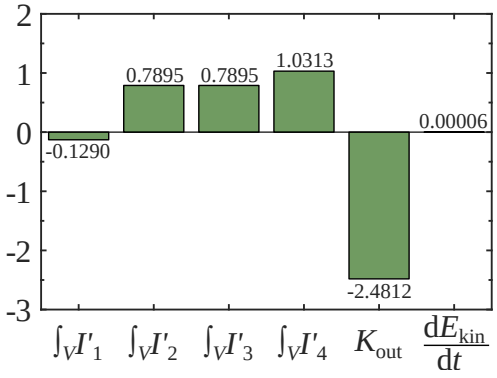

FIG. 21. Integral energy budget.

The lift-up effect is a typical destabilization mechanism proper of shear flows, and in our case it plays a significant role because the basic state streamlines are logarithmic spirals, hence a fluid element would be subject to a shear if displaced in cross-stream direction. On the other hand, the streamwise deceleration is a destabilizing mechanism dominant in all the diffusers and jet flows. It seems, therefore, that centrifugal instabilities do not play any significant role within the model framework. To confirm it, we apply the criterion by Sipp and Jacquin [33] that identifies the necessary condition to admit centrifugal instabilities for inviscid, incompressible, two-dimensional planar flows in rotating systems. Their criterion generalized the Rayleigh criterion by considering the local algebraic radius of curvature $\ddot{R}$ at a given point of a basic state streamline:

$$\ddot{R} = \frac{|\vec{U}_0|^3}{(\nabla\psi_0)\cdot[\vec{U}_0\cdot\nabla\vec{U}_0]}, \tag{22}$$

where ψ_0 is the basic state stream function. The criterion of Sipp and Jacquin [33] is defined on the following quantity:

$$\delta = 2\left(\frac{|\vec{U}_0|}{\ddot{R}} + \Omega\right)(\nabla\times\vec{U}_0 + 2\Omega), \tag{23}$$

where Ω denotes the rotation rate of the coordinate system, i.e. $\Omega = 0$ in our case. According to Sipp and Jacquin [33], the flow is unstable if there exists ψ_0 such as $\max_{\psi_0}(\delta) < 0$. Reworking our basic steady, the terms entering the local algebraic radius of curvature can be computed as

$$U_{0,r} = \frac{1}{r}\frac{\partial\psi_0}{\partial\theta}, \qquad U_{0,\theta} = -\frac{\partial\psi_0}{\partial r}, \tag{24}$$

then it yields

$$\nabla\psi_0 = \left[\frac{\partial\psi_0}{\partial r} \;\; \frac{1}{r}\frac{\partial\psi_0}{\partial\theta}\right] = \left[-U_{0,\theta} \;\; U_{0,r}\right] = \left[-\frac{\mu}{r} \;\; \frac{1}{r}\right], \tag{25}$$

and we can calculate

$$\begin{aligned}(\nabla\psi_0)\cdot[\vec{U}_0\cdot\nabla\vec{U}_0] &= \left[-\frac{\mu}{r} \;\; \frac{1}{r}\right]\cdot\begin{bmatrix} U_{0,r}\dfrac{\partial U_{0,r}}{\partial r} - \dfrac{U_{0,\theta}^2}{r} \\ U_{0,r}\dfrac{\partial U_{0,\theta}}{\partial r} + \dfrac{U_{0,r}U_{0,\theta}}{r}\end{bmatrix} \\ &= \frac{\mu}{r^4}(1+\mu^2).\end{aligned} \tag{26}$$

Finally $|\vec{U}_0|^3 = \frac{1}{r^3}(\mu^2+1)^{\frac{3}{2}}$, and it yields

$$\ddot{R} = \frac{r}{\mu}\sqrt{\mu^2+1}. \tag{27}$$

Hence, the final form of δ reads

$$\delta = \frac{2\mu\nabla\times\vec{U}_0}{r^2}. \tag{28}$$

since our basic state is irrotational, i.e. $\nabla\times\vec{U}_0 = 0$, the flow is always neutrally stable to the centrifugal instability. This means that the necessary condition to attribute the instability to a Rayleigh centrifugal-type mechanism is not met under the simplifying hypotheses of the model of Tsujimoto, Yoshida, and Mori [8], hence our instability is not centrifugal.

Considering that $|U_z| \ll |U_r|,\ |U_\theta|$ in our URANS simulations, the two-dimensional criterion of Sipp and Jacquin [33] is applied to the mid-height diffuser flow of our full-pump results. The low-flow-rate rotating stall is expected to occur at $Q \approx 0.6Q_d$ [34], hence we computed δ and the in-plane streamlines at $z = 0$ for $Q/Q_d = 0.5$ (fig. 22(a)) and 0.75 (fig. 22(b)). As all the in-plane streamlines (black lines) pass through regions of positive δ (gray zones), hence none of them verifies the necessary condition $\max_{\psi_0}\delta < 0$ to admit the centrifugal instability as a destabilizing mechanism. We consider

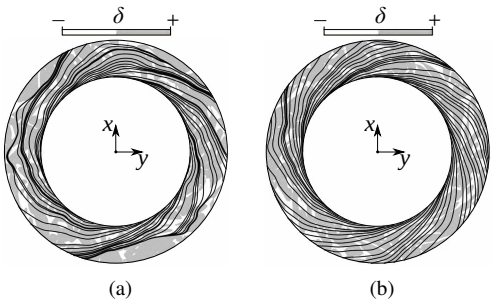

(a) (b)

FIG. 22. Numerically calculated δ at the mid-height (z = 0) of the diffuser at flow rate (a) $Q/Q_d = 0.50$, and (b) $Q/Q_d = 0.75$ obtained from the URANS simulation. The black lines denote the in-plane streamlines at $z = 0$.

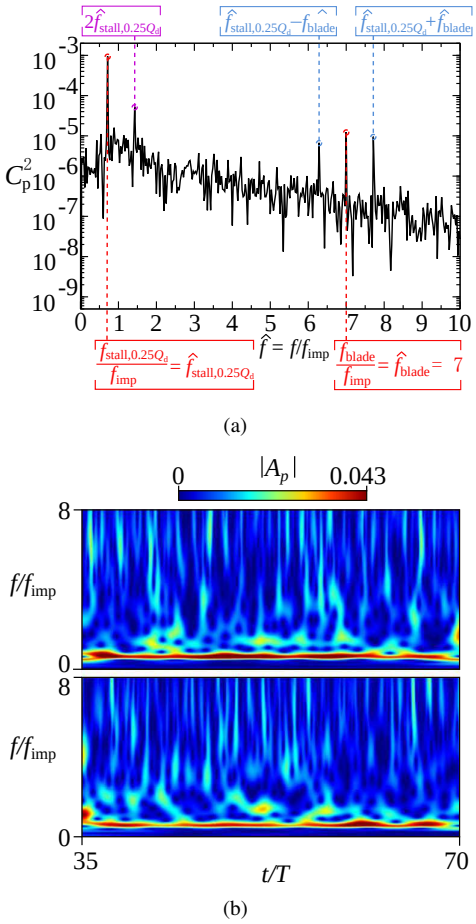

FIG. 23. (a) Fourier and (b) wavelet analysis of the URANS simulation of the zero-leakage case at the stall condition Q/Q_{d} =0.25.

this as an heuristic indication that the rigorous proof derived for the Tsujimoto's model can be generalized to the three-dimensional diffuser flow.

2. *Rotating stall characteristics of the zero-leakage case*

To capture and visualize the unsteady flow field associated with the rotating stall at low flow rates, fig. 23 shows the FFT and wavelet analysis of the URANS simulations for the zero-leakage case at fully-developed stall conditions for $Q/Q_{\mathrm{d}} = 0.25$. The frequency associated with the low-flow-rate rotating stall $f_{\mathrm{stall},0.25Q_{\mathrm{d}}}/f_{\mathrm{imp}} = 0.714$ and the blade passing frequency $f_{\mathrm{blade}}/f_{\mathrm{imp}} = 7$ can be identified very clearly as shown in fig. 23(a). The FFT identifies therefore the propagation velocity of the stall cells $\omega_{\mathrm{stall},0.25Q_{\mathrm{d}}} = 0.238\omega_{\mathrm{imp}}$. Moreover, the non-linear interaction between such two frequencies is also observed in the FFT at $f_{\mathrm{stall},0.25Q_{\mathrm{d}}} + f_{\mathrm{imp}}$. The rotating stall frequency can also be clearly identified by the wavelet analysis as shown in fig. 23(b).

Figure 24 shows the phase averaged color maps with 120-time steps of the last revolution at the mid-height of the diffuser in a reference frame rotating with the rotating stall propagation velocity $\omega_{\mathrm{stall},0.25Q_{\mathrm{d}}}$. Three cells are clearly identified (top) and they qualitatively well compared with the critical mode predicted by linear stability analysis within the model of Tsujimoto (bottom). They are composed of two regions of inward and outward radial velocities located near the diffuser inlet, and between these two regions a zone with negative tangential velocity is identified.

3. *Comparison of different cases at low-flow-rate stall conditions*

Numerical simulations at fully-developed stall conditions will be compared for the three different pump geometries of interest in this study. Figure 25 presents the comparison of the Fourier and wavelet analysis for the URANS simulations and experiments at $Q/Q_{\mathrm{d}} = 0.25$. For the zero-leakage case (fig. 25 (a)), the rotating stall instability frequency was captured both by the Fourier and wavelet analysis as described before. This is also the case for the negative-leakage case (fig. 25(b)), whose instability frequency are similar to the ones found for the zero-leakage case. For the positive-leakage case (fig. 25(c)), the leakage flow has a significant impact on the rotating stall characteristics in the vaneless diffuser. The FFTs are qualitatively similar, but the wavelet analysis demonstrates a significant difference with respect to the zero- and negative-leakage cases (fig. 25(a–d)). In the URANS simulations for the positive-leakage case at $Q/Q_{\mathrm{d}} = 0.25$, the impeller–diffuser leakage is larger than in the experiments, and the leakage flow (rotating with the impeller walls) enters the diffuser with the impeller frequency f_{imp}, resulting in non-linear interactions with the blade passing frequency f_{blade} and the rotating stall frequency $f_{\mathrm{stall},0.25Q_{\mathrm{d}}}$, triggering a more complicated flow field.

Table IV summarizes the numerical and experimental results derived from the corresponding FFTs. One can observe that the stall propagation velocity $\omega_{\mathrm{stall},0.25Q_{\mathrm{d}}}$ identified in the different cases is compatible with the experimental one. However, the rotating instability frequency is very sensitive to the leakage flow. To illustrate this effect, fig.

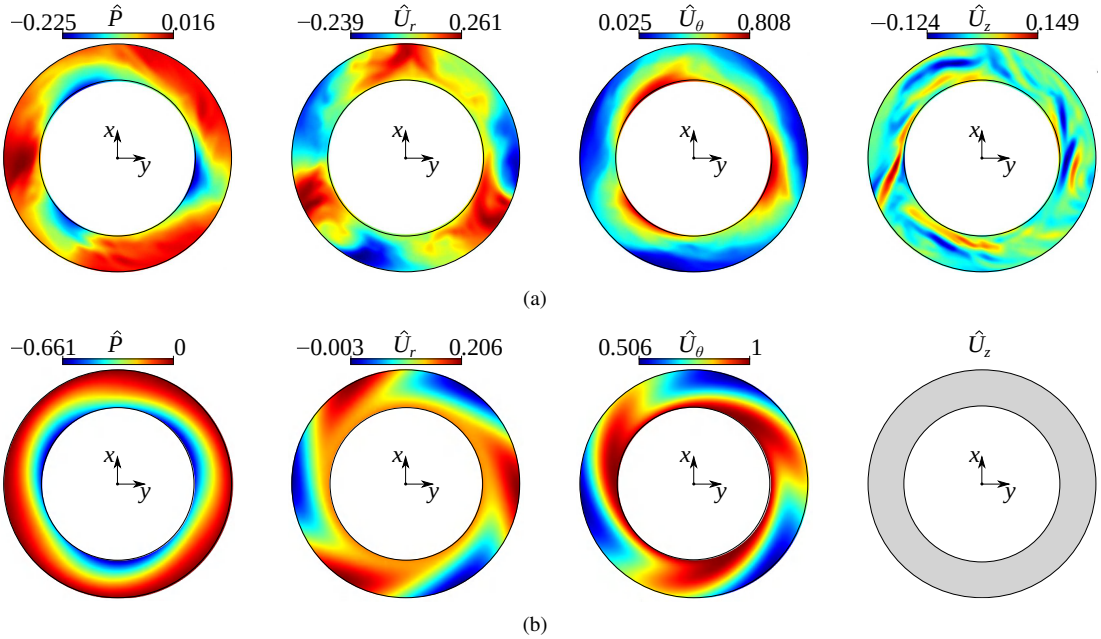

FIG. 24. Comparison of (a) the phase averaged static pressure, radial velocity, tangential velocity and axial velocity with the instability propagation velocity $\omega_{\text{stall},0.25Q_\text{d}}$ of the zero-leakage case at stall condition $Q/Q_\text{d} = 0.25$ of the URANS simulation, and (b) the flow field calculated by the 2D linear stability model of Tsujimoto, Yoshida, and Mori [8] at the critical condition.

TABLE IV. Propagation velocity of the rotating instability obtained by the FFT at the stall condition Q/Q_d = 0.25.

Case	Zero-leakage (URANS)	Negative-leakage (URANS)	Positive-leakage (URANS)	Positive-leakage (Experiment)	2D linear model (Tsujimoto)
$f_{\text{stall},0.25Q_\text{d}}/f_\text{imp}$	0.714	0.686	0.486	0.840	0.867
$\omega_{\text{stall},0.25Q_\text{d}}/\omega_\text{imp}$	0.238	0.228	0.162	0.280	0.289

26 depicts the change of the rotating stall frequencies (fig. 26(a)) and amplitudes (fig. 26(b)) extracted from all simulations and experiments plotted against the effective diffuser flow rate Q_D/Q_d (corrected taking into account the leakage flow) normalized to the nominal flow rate Q_d. The instability frequency decreases upon an increase of the effective diffuser flow rate and $f_{\text{stall},0.25Q_\text{d}}/f_\text{imp} \approx \alpha + \beta Q_\text{D}$, where $\alpha = 0.9689$ and $\beta = -0.8189$ are fitting coefficients that approximate at leading order the change of frequency with Q_D for all the pump configurations considered in this study. The critical diffuser flow rate can be estimated assuming that the rotating stall instability is strongly driven by a linear process as described in Sec. IV E 1. This brings to assume that the square of the perturbation amplitude scales with the deviation of Q_D from the critical flow rate $Q_\text{D,c}$, i.e. $C_p^2 \sim (Q_\text{D} - Q_\text{D,c})$. Extracting C_p^2 from the FFT for $Q/Q_\text{d} = 0.25$ and 0.5, $Q_\text{D,c}$ can be approximated by linear extrapolation up to $C_p^2 = 0$, as shown by the dashed lines in fig. 26(b). Three values of $Q_\text{D,c}$ are found, one per each leakage configuration considered, i.e. zero-, negative-, and positive-leakage. The critical values numerically estimated by our URANS all fall within the experimental range $Q_\text{D,c} \in [0.55,\ 0.7]$ measured by looking for local recirculation regions, as reported by Barrand, Caignaert, and Canavelis [34] in the very first publication on the present pump model. The good agreement between numerics and experiments on the critical onset is depicted in fig. 26(b).

Figure 27 depicts the normalized rotation frequency of the rotating stall resulting from the URANS simulations and Tsujimoto's model. The comparison between these data demonstrates that the critical angle α_c predicted by Tsujimoto's model (magenta triangle) is in good agreement with the α of the closest-to-critical rotating stall conditions we found, i.e. $\alpha_c \approx \alpha(Q/Q_\text{d} = 0.5,\ \text{positive-leakage case})$. We however remark that the simplified model of Tsujimoto significantly over-predicts the critical propagation velocity by about a factor of 3.

Figure 28 shows the comparison of the phase-averaged flow field in a reference frame rotating with the rotating stall propagation velocity. According to fig. 26, the experimental PIV measurements for $Q = 0.26Q_\text{d}$ (fig. 28(d), (Dazin [12])) are best compared with the phase-averaged flow field for the zero- and negative-leakage cases ($Q = 0.25Q_\text{d}$, fig. 28(a,b)). As the positive-leakage case (fig. 28(c)) considers an effective flow rate of $Q_\text{D} = 0.43Q_\text{d}$, the phase-averaged rotating stall is not

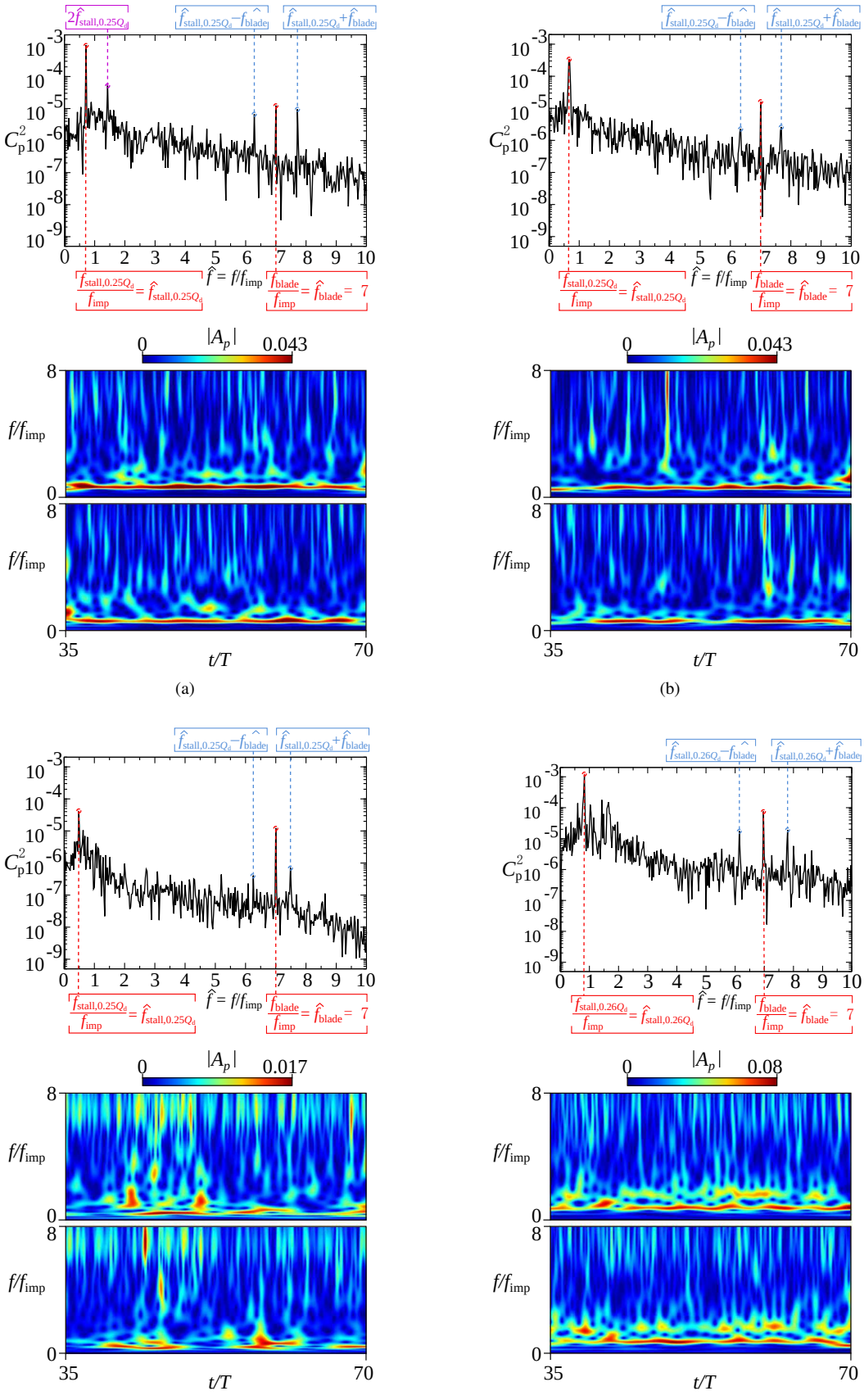

FIG. 25. Fourier and wavelet analysis of the URANS simulation for (a) the zero-leakage case, (b) the negative-leakage case, and (c) the positive-leakage case, and of (d) the experiment, at the stall condition $Q/Q_{\mathrm{d}} = 0.25$.

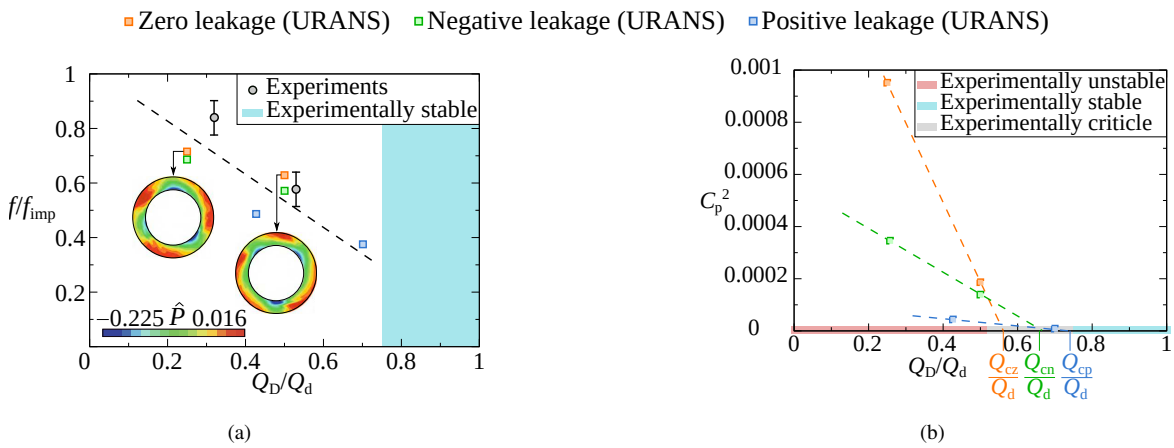

(a) (b)

FIG. 26. (a) Rotating stall frequency and (b) amplitude analysis at small flow rates ($Q/Q_d = 0.50$ and 0.25).

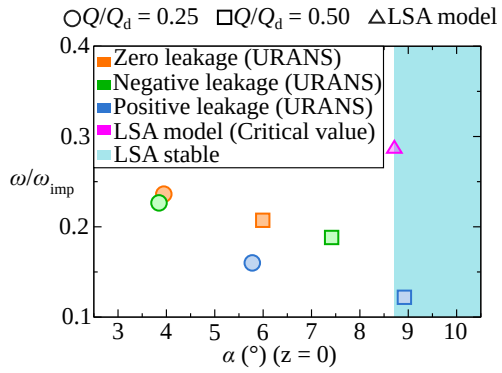

FIG. 27. Flow angle of the core flow versus rotating stall propagation velocity at small flow rates ($Q/Q_d = 0.50$ and 0.25).

comparable to the other cases which have the same nominal flow rate $Q = 0.25Q_d$. Three stall cells are identified in the phase-averaged URANS for the zero- and negative-leakage cases, and they qualitatively and quantitatively well compare in terms of the velocity field with the PIV experimental measurements.

V. SUMMARY AND CONCLUSIONS

The flow field in a centrifugal pump was thoroughly investigated by combining URANS simulations, theoretical modeling, and experiments. Among the major focuses of this study is the investigation of the leakage effect produced by a radial gap between the impeller and the vaneless diffuser. Hence, three geometries have been considered: (i) a zero-leakage case (ideal case commonly simulated in literature), a positive-leakage case (corresponding to our experimental facility), and (iii) a negative-leakage case (most commonly employed in industrial applications).

The numerical simulations have first been validated by comparing them with corresponding experiments. The URANS-predicted pump and diffuser performances are in very good agreement with the experimental measurements, with a maximum error of about 5% observed for the zero- and positive-leakage cases. Moreover, the onset and features of the low-flow-rate rotating stall observed in the experiments have well been reproduced by our URANS simulations. The validated numerical tool has therefore been used to investigate more in-depth the rotating instabilities occurring in the vaneless diffuser for the three aforementioned configurations, taking the ideal case (i.e. the zero-leakage case) as a reference.

We identified, for the first time in this centrifugal pump, an unexpected rotating instability occurring in the vaneless diffuser at design flow rate $Q = Q_d$. This rotating stall has a major impact on the mean flow and it is responsible for a large separation region on the diffuser hub. As a result, the diffuser performance significantly degrades. The instability mechanism has been traced back to the two-dimensional jet-wake instability reported by Ljevar, de Lange, and van Steenhoven [10], verifying that we get a parametric onset of the instability, as well as a wavenumber consistent with their predictions.

Moreover, by means of dedicated wavelet analysis, we identified a secondary instability pulsating in the reference frame of the primary rotating stall and migrating from the shear layer of the impeller wake to the diffuser outlet. To the best of the authors' knowledge, this secondary instability has been reported in our study for the first time. The same rotating stall has been found for the negative-leakage case at the design flow rate, however, the disturbance due to the entrainment of the leakage flow was strong enough to almost totally disrupt the secondary instability, even if a clear signature of it remains in the wavelet analysis. On the contrary, when a positive-leakage case is considered, the modification to the jet-wake angle brings the flow into the stable regime and no rotating stall is observed. This is in agreement with the prediction of the two-dimensional model of Ljevar, de Lange, and van Steenhoven [10] and it is confirmed by our experiments. A corresponding suppression of the separation region over the diffuser hub is observed, leading to a significant increase in the diffuser performance (also confirmed by our experiments).

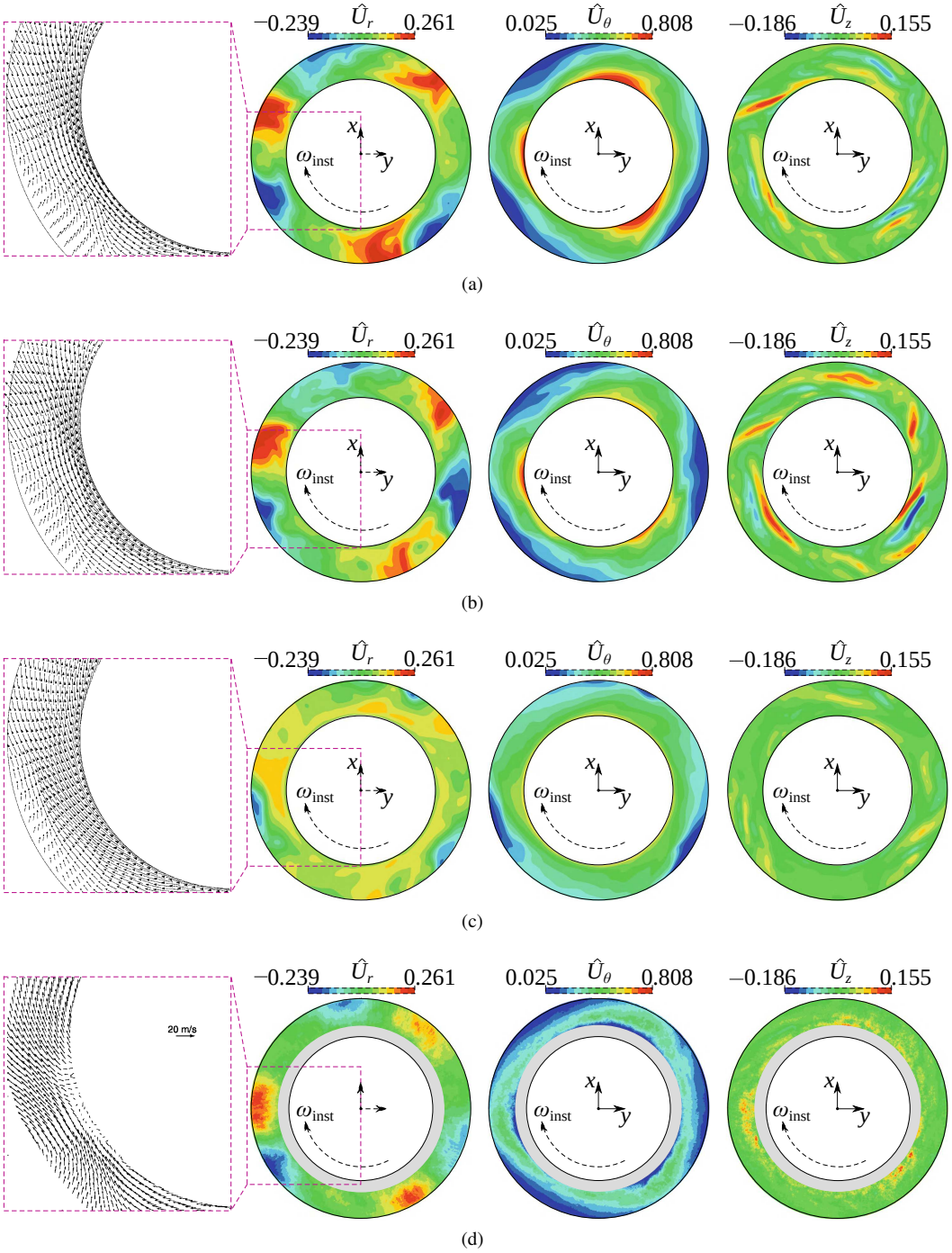

FIG. 28. Phase averaged velocity vectors and color maps of radial, tangential, and axial velocity at the mid-height of the diffuser based on the instability propagation speed $\omega_{\text{stall},0.25Q_d}$ at the stall condition $Q/Q_d = 0.25$ for (a) the zero-leakage case, (b) the positive-leakage case, (c) the negative-leakage case, and (d) the PIV measurement results. The grey region close to the diffuser inlet is not accessible to PIV because of laser reflection on the impeller blades. The measurements near its edge are therefore to be considered affected by a significant error bar.

This leads to the remarkable conclusion that even small radial gaps between the impeller and the diffuser, as the 1% gap we consider, can significantly affect the flow and they must be included in the pump design when numerical shape optimization is performed.

By varying the flow rate from $Q = 1.25Q_d$ down to $Q = 0.25Q_d$, we bracketed the design-flow rate instability to the range above $Q > 0.75Q_d$ and below $Q < 1.25Q_d$. Moreover, we found another rotating instability for $Q < 0.65Q_d$. This low-flow-rate rotating stall has been previously reported in the literature by several authors (see e.g. Dazin [12]), and a good agreement is found also in terms of the instability on-

set (Barrand, Caignaert, and Canavelis [34] reports an onset at $Q \approx 0.6Q_d$). The rotating stall has been characterized numerically for our three leakage configurations and good qualitative and quantitative agreement was demonstrated in comparison with the PIV measurements reported in the literature and with the FFT and wavelet analysis performed on our experiments.

An in-depth theoretical analysis has been carried out to shed some light on the mechanisms at the core of this instability. Employing the two-dimensional, inviscid model of Tsujimoto, Yoshida, and Mori [8], we demonstrated that a consistent $m = 3$ critical mode is predicted by linear stability analysis assuming that the flow is homogeneous in θ. Furthermore, by arbitrarily scaling the critical perturbation and superposing it to the basic state of Tsujimoto's model, it has been shown a remarkably good agreement with our URANS phase-averaged results for supercritical conditions. This supports the conclusion that the rotating stall emerges from a core-flow instability and it does not get significantly influenced by the presence of the turbulent boundary layers on the shroud and on the hub of the diffuser.

We point out that, even though both the rotating stalls are core-flow instabilities, they are essentially different because the low-flow-rate stall does not require a jet-wake inflow, but it rather relies on the skewness of the flow at the diffuser inlet. Finally, by carrying out an energy budget analysis on the critical perturbation, we demonstrated for the first time that the low-flow-rate instability is produced by the contribution of lift-up and flow deceleration mechanisms; moreover, we ruled out the hypothesis of a centrifugal-type mechanism as an origin for the rotating stall.

DATA AVAILABILITY

The data that support the findings of this study are available from the corresponding author upon reasonable request.

ACKNOWLEDGEMENTS

We kindly acknowledge the GENCI (Grand Equipement National de Calcul Intensif) for the numerical resources granted to conduct this study under project A0102A01741. Furthermore, we appreciate the support of the China Scholarship Council for the doctoral students of M. Fan (CSC student number 201908320328).

Appendix A: OpenFOAM solvers

The open-source software OpenFOAM v1912 has been used to carry out all the numerical simulations of this study. An overview of the applied algorithms and discretization schemes used in our numerical simulations is shown in tab. V. For the RANS simulations the solver `simpleFoam` is employed, making use of Multiple Reference Frames (MRF) to deal with fixed and rotating boundaries (matched using a mixing plane technique[35]), while the transient solver `pimpleFoam` was used for the URANS simulations, employing a dynamic mesh to handle the pump without using a mixing plane[36].

To solve the discretized systems, the option `smoothSolver` was used along with the linear solver `GaussSeidel smoother` for velocity and all transported variables. For pressure, the `GAMG` solver was employed together with the linear solver `symGaussSeidel smoother` (Behrens [37], Greenshields [38]). The pressure–velocity coupling is taken care of by the OpenFOAM Rhie–Chow interpolation[39] in combination with the Semi-Implicit Method for Pressure Linked Equations (SIMPLE) algorithm for steady calculations, whereas the Pressure-Implicit Method for Pressure Linked Equations (PIMPLE) algorithm is used for the URANS. The latter is a combination of the Pressure-Implicit with Splitting of Operators (PISO) and the SIMPLE algorithms allowing for larger time steps (Greenshields [38], Uroić [40]) than the standard PISO algorithm. The PIMPLE algorithm is set to operate with three inner loops, one nonorthogonal, and two outer corrector loops. The under-relaxation factors of pressure, momentum, turbulent kinetic energy, and turbulent dissipation rate for RANS simulation are set to 0.4, 0.6, 0.3, and 0.3, respectively. For the URANS simulation, the under-relaxation factors of momentum, turbulent kinetic energy, and turbulent dissipation rate are set to 0.7.

The temporal discretization terms are discretized using a second–order backward differentiation scheme (`backward` option in OpenFOAM). For the gradient terms, the discretization scheme employs a second–order discretization with Gaussian interpolation (option `Gauss` in OpenFOAM), while linear interpolation is employed to consistently reconstruct the flow inside the finite volumes. The divergence term in the projected momentum equation is discretized using a second-order upwind scheme (`linearUpwind` in OpenFOAM), which is a blend of linear and upwind schemes. The Gauss linear corrected scheme is used for the Laplacian terms and a linear interpolation is employed for reconstructing velocity and pressures in the finite volume cells from their face fluxes. Finally, for the RANS simulations, the steady state is assumed to be converged if the residuals of mass, momentum, and turbulence properties become smaller than 5×10^{-4}.

Appendix B: Mesh independence analysis

A grid number independence verification was carried out with four grids. Table VI shows the comparison of the predicted mass-weighted average static pressure difference between the pipe inlet and the diffuser outlet (PSI) of the centrifugal pump at the design condition with different grid resolutions. The relative error of the predicted pump performance increases with the increase of the grid size passing from 618k cells (Grid 1) to ≈1.1M cells (Grid 2) and then decreased to 0.93% for 2.3M cells (Grid 3). Therefore, a total mesh number of 2.3M finite volumes was selected for the numerical simulations.

Appendix C: Flow field details for $Q/Q_{\mathrm{d}} = 1$

Color maps of the instantaneous static pressure, radial velocity, tangential velocity, and axial velocity at the design flow rate $Q/Q_{\mathrm{d}} = 1.00$ for (a) the zero-leakage case, (b) the negative-leakage case, and (c) the positive-leakage case. The upper figures show the azimuth averaged value on the meridian section of the diffuser, the lower figures show the instantaneous value at the mid-height of the diffuser.

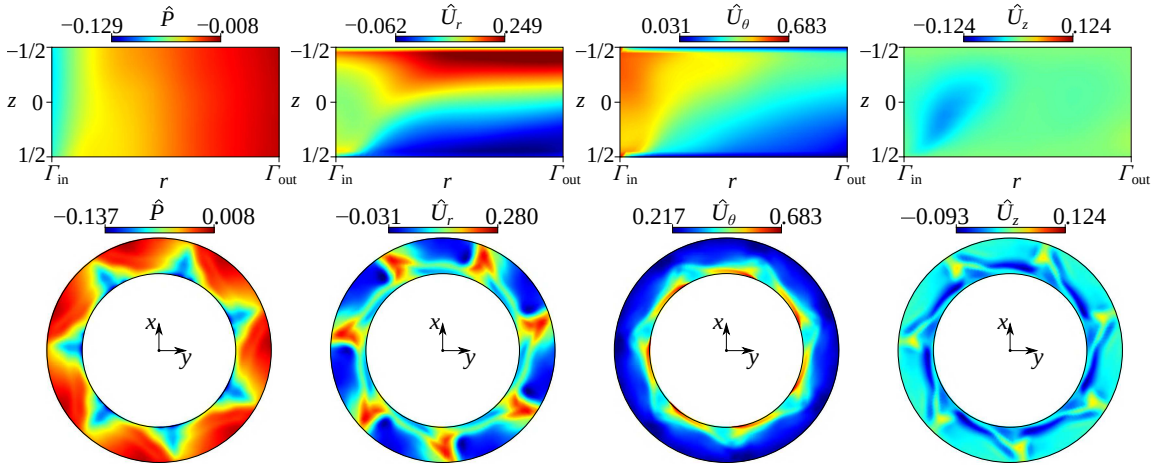

(a)

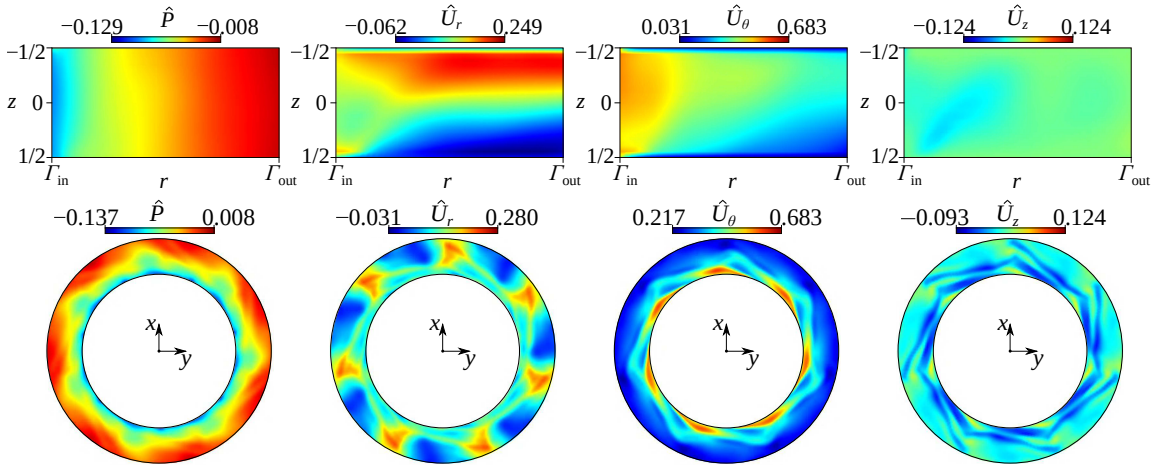

(b)

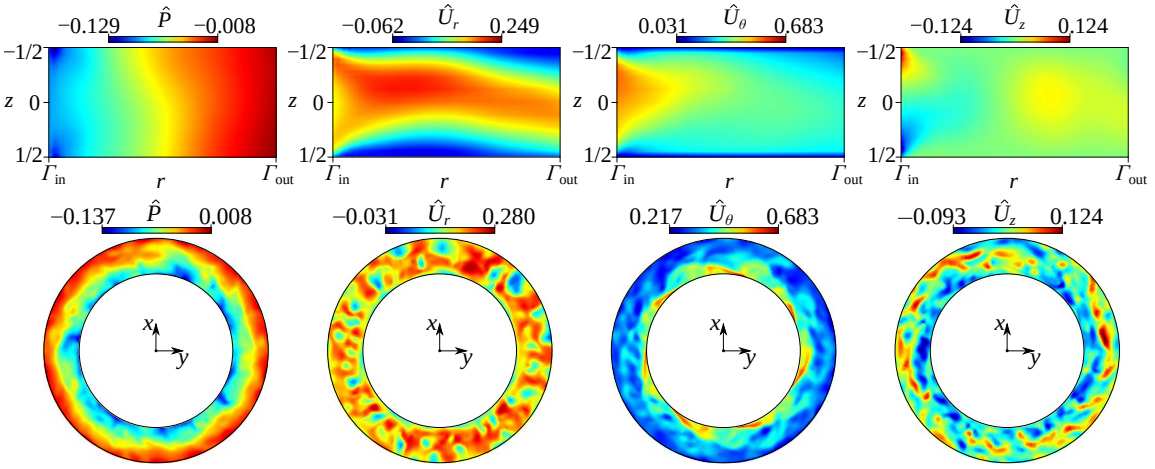

(c)

TABLE V. Numerical methods and schemes employed in OpenFOAM v1912.

Types	RANS	URANS
Numerical method		
Solver	simpleFoam	pimpleFoam
Pressure-velocity coupling	SIMPLE	PISO
Matrices-solver	p: `GAME`; U,k,ω: `smoothSolver`	p: `GAME`; U,k,ω: `smoothSolver`
Relaxation factor	$p:0.5$; $U:0.8$; $k,\omega:0.7$	$U,k,\omega:0.7$
Discretization scheme		
Time	`steadyState`	`backward`
Gradient	`Gauss linear`	`Gauss linear`
Divergence	`Gauss linearUpwind`	`Gauss linearUpwind`
Laplacian	`Gauss linear corrected`	`Gauss linear corrected`
Interpolation	`linear`	`linear`

TABLE VI. Grid independence verification data. δ is the relative error computed with respect to the finest grid, i.e. $\delta = |\mathrm{PSI}_{\mathrm{Case\ 4}} - \mathrm{PSI}_{\mathrm{Case}\ *}|/|\mathrm{PSI}_{\mathrm{Case\ 4}}|$, where PSI denotes the mass-weighted average static pressure difference between the pipe inlet and the diffuser outlet, the asterisk denotes either Grid 1, 2 or 3.

Grid #	Cells number					PSI	δ
	inlet pipe	impeller	diffuser	outflow box	total		
1	113155	267008	145728	91800	617691	0.3843	1.75%
2	238853	493920	210600	175446	1118819	0.3864	2.30%
3	406462	1051176	590976	267786	2316400	0.3742	0.93%
4	1218825	2456160	1379448	352350	5406783	0.3777	–

[1] D. Japikse, "Stall, stage tage stall, and surge," Proceedings of the Tenth Turbomachinery Symposium. Texas A&M University. Turbomachinery Laboratories (1981).

[2] W. Jansen, "Rotating Stall in a Radial Vaneless Diffuser," Journal of Basic Engineering **86**, 750–758 (1964).

[3] Y. Senoo and Y. Kinoshita, "Influence of inlet flow conditions and geometries of centrifugal vaneless diffusers on critical flow angle for reverse flow," journal of Fluids Engineering, Trans. ASME , 98–102 (1977).

[4] Y. Senoo, Y. Kinoshita, and M. Ishida, "Asymmetric flow in vaneless diffusers of centrifugal blowers," journal of Fluids Engineering, Trans. ASME , 104–114 (1977).

[5] A. N. Abdelhamid, W. H. Colwill, and J. F. Barrows, "Experimental investigation of unsteady phenomena in vaneless radial diffusers," Journal of Engineering for Power **101**, 52–59 (1979).

[6] A. N. Abdelhamid, "Effects of vaneless diffuser geometry on flow instability in centrifugal compression systems," Turbo Expo: Power for Land, Sea, and Air **101**, 79610, p. V001T03A008 (1981).

[7] P. Frigne and R. Van den Braembussche, "A Theoretical Model for Rotating Stall in the Vaneless Diffuser of a Centrifugal Compressor," Journal of Engineering for Gas Turbines and Power **107**, 507–513 (1985).

[8] Y. Tsujimoto, Y. Yoshida, and Y. Mori, "Study of Vaneless Diffuser Rotating Stall Based on Two-Dimensional Inviscid Flow Analysis," Journal of Fluids Engineering **118**, 123–127 (1996).

[9] Y. Heng, A. Dazin, and M. Ouarzazi, "Linear stability analysis of rotating stall in a wide vaneless diffuser," in *12th European Conference on Turbomachinery Fluid Dynamics and Thermodynamics, ETC 2017* (2017).

[10] S. Ljevar, H. C. de Lange, and A. A. van Steenhoven, "Two-dimensional rotating stall analysis in a wide vaneless diffuser. international journal of rotating machinery," International Journal of Rotating Machinery **2006**, 1—-11 (2006).

[11] G. Pavesi, A. Dazin, G. Cavazzini, G. Caignaert, G. Bois, and G. Ardizzon, "Experimental and numerical investigation of unforced unsteadiness in a vaneless radial diffuser," in *9th European Conference on Turbomachinery: Fluid Dynamics and Thermodynamics, ETC 2011 - Conference Proceedings*, Vol. 1 (2011).

[12] A. Dazin, "High-speed stereoscopic piv study of rotating instabilities in a radial vaneless diffuser," Experiments in Fluids **51**, 83–93 (2011).

[13] G. Wuibaut, G. Bois, P. Dupont, G. Caignaert, and M. Stanislas, "PIV Measurements in the Impeller and the Vaneless Diffuser of a Radial Flow Pump in Design and Off-Design Operating Conditions," Journal of Fluids Engineering **124**, 791–797 (2002).

[14] A. Dazin, O. Coutier-Delgosha, P. Dupont, S. Coudert, G. Caignaert, and G. Bois, "Rotating instability in the vaneless diffuser of a radial flow pump," Journal of Thermal Science **17** (2008), 10.1007/s11630-008-0368-3.

[15] D. C. Wilcox, *Turbulence Modeling for CFD* (DCW Industries, 1993).

[16] P. Sváček, P. Louda, and K. Kozel, "On numerical simulation of three-dimensional flow problems by finite element and finite volume techniques," Journal of computational and applied mathematics **270**, 451–461 (2014).

[17] F. R. Menter, J. C. Ferreira, T. Esch, and B. Konno, "The sst turbulence model with improved wall treatment for heat transfer predictions in gas turbines," Gas Turnine Congress (International) Proceedings. Tokyo. **IGTC2003**, 059 (2003).

[18] M. Rahman, "Numerical investigation of unsteady flow past a circular cylinder using 2-d finite volume method," Journal of Naval Architecture and Marine Engineering **4(1)**, 27–42 (2008).

[19] F. R. Menter, "Ten years of industrial experience with the sst turbulence model," Turbulence, heat and mass transfer **4**, 625–632 (2003).

[20] L. Gibson, L. Galloway, and S. Spence, "Assessment of turbulence model predictions for a centrifugal compressor simulation," Journal of the Global Power and Propulsion Society **1**, 142–156 (2017).

[21] I. Chalghoum, H. Kanfoudi, S. Elaoud, M. Akrout, and R. Zgolli, "Numerical modeling of the flow inside a centrifugal pump: Influence of impeller–volute interaction on velocity and pressure fields," Arabian journal for science and engineering **41(11)**, 4463–4476 (2016).

[22] O. Borm and H. P. Kau, "Unsteady aerodynamics of a centrifugal compressor stage: Validation of two different cfd solvers," In Turbo Expo: Power for Land, Sea, and Air **44748**, 2753–2764 (2012).

[23]J. H. Kim, J. H. Choi, and K. Y. Kim, "Design optimization of a centrifugal compressor impeller using radial basis neural network method," In Turbo Expo: Power for Land, Sea, and Air **48883**, 443–451 (2009).
[24]M. Asuaje, F. Bakir, S. Kouidri, F. Kenyery, and R. Rey, "Numerical modelization of the flow in centrifugal pump: volute influence in velocity and pressure fields," International journal of rotating machinery **3**, 244–255 (2005).
[25]M. Invigorito, D. Cardillo, and G. Ranuzzi, "Application of openfoam for rocket design," In 9th OpenFOAM Workshop , 1–15 (2003).
[26]C. Hu, "Investigation of rotating stall in radial vaneless diffusers with asymmetric inflow," Aerospace Science and Technology **96**, 105546 (2020).
[27]M. Šourek and M. Isoz, "Dem-cfd study of flow in a random packed bed," Conference TOPICAL PROBLEMS OF FLUID MECHANICS (2018).
[28]F. Cenci and A. L. C. Fujarra, "Urans simulation: numerical study of flow around a two dimensional circular cylinder," Proceedings of the XXXVIII Iberian Latin-American Congress on Computational Methods in Engineering (2017).
[29]Y. G. Heng, A. Dazin, M. N. Ouarzazi, and Q. R. Si, "Experimental study and theoretical analysis of the rotating stall in a vaneless diffuser of radial flow pump," in *IOP Conference Series: Earth and Environmental Science*, Vol. 49 (2016) p. 032006.
[30]Y. G. Heng, A. Dazin, M. N. Ouarzazi, and Q. R. Si, "A study of rotating stall in a vaneless diffuser of radial flow pump," Journal of Hydraulic Research **56(4)**, 494–504 (2018).
[31]S. Suzuki, U. Yoshio, and H. H., "Noise characteristics in partial discharge of centrifugal fans: 1st report, low-frequency noise due to the rotating stall." Bulletin of JSME **21(154)**, 689–696 (1978).
[32]G. Caignaert, B. Desmet, and D. Stevenaert, "Experimental investigations on the flow in the impeller of a centrifugal fan." In Turbo Expo: Power for Land, Sea, and Air (Vol. 79566, p. V001T01A013).American Society of Mechanical Engineers. (1982).
[33]D. Sipp and L. Jacquin, "Three-dimensional centrifugal-type instabilities of two-dimensional flows in rotating systems," Physics of Fluids **12(7)**, 1740–1748 (2000).
[34]J. Barrand, G. Caignaert, and R. Canavelis, "Experimental determination of the reverse flow onset in a centrifugal impeller." In Proceedings of the 1st International Pump Symposium. Turbomachinery Laboratories, Department of Mechanical Engineering, Texas A&M University. (1984).
[35]D. Wilhelm, "Rotating flow simulations with openfoam," International Journal of Aeronautical Science & Aerospace Research **1**, 001 (2015).
[36]D. Živković, *Simulacija promjene opterećenja Francisove hidrauličke turbine*, Master's thesis, University of Zagreb, Zagreb (2016).
[37]T. Behrens, "Openfoam's basic solvers for linear systems of equations," Tech. Rep. 1802 (Chalmers, Department of Applied Mechanics, 2009).
[38]C. J. Greenshields, *OpenFOAM user guide*, The OpenFOAM Foundation (2020).
[39]H. Jasak, *Error analysis and estimation for the finite volume method with applications to fluid flows*, Ph.D. thesis, University of London, London (1996).
[40]T. Uroić, *Implicitly coupled finite volume algorithms*, Ph.D. thesis, University of Zagreb, Zagreb (2019).